

Virtual and Physical Prototyping

ISSN: 1745-2759 (Print) 1745-2767 (Online) Journal homepage: www.tandfonline.com/journals/nvpp20

Robot-assisted multi-axis embedded silicone printing for free-form volumetric model

Hailin Sun, Yingjun Tian, Chenyu Xu, Mahdi Bodaghi, Fei Gao & Guoxin Fang

To cite this article: Hailin Sun, Yingjun Tian, Chenyu Xu, Mahdi Bodaghi, Fei Gao & Guoxin Fang (2026) Robot-assisted multi-axis embedded silicone printing for free-form volumetric model, *Virtual and Physical Prototyping*, 21:1, e2614811, DOI: [10.1080/17452759.2026.2614811](https://doi.org/10.1080/17452759.2026.2614811)

To link to this article: <https://doi.org/10.1080/17452759.2026.2614811>



© 2026 The Author(s). Published by Informa UK Limited, trading as Taylor & Francis Group



Published online: 16 Jan 2026.



Submit your article to this journal



Article views: 331



View related articles



View Crossmark data

Robot-assisted multi-axis embedded silicone printing for free-form volumetric model

Hailin Sun  ^a, Yingjun Tian  ^b, Chenyu Xu  ^a, Mahdi Bodaghi  ^c, Fei Gao  ^d and Guoxin Fang  ^{a,e}

^aDepartment of Mechanical and Automation Engineering, The Chinese University of Hong Kong, Hong Kong, People's Republic of China;

^bDepartment of Mechanical and Aerospace Engineering, The University of Manchester, Manchester, UK; ^cDepartment of Engineering, School of Science and Technology, Nottingham Trent University, Nottingham, UK; ^dShenzhen Institute of Advanced Technology, Chinese Academy of Sciences, Shenzhen, People's Republic of China; ^eInstitute of Intelligent Design and Manufacturing, The Chinese University of Hong Kong, Hong Kong, People's Republic of China

ABSTRACT

Embedded silicone printing (ESP) enables the creation of complex soft structures by extruding silicone inks into a gel support matrix. However, issues such as excess local ink deposition and the staircase effect limit the quality of solid model prints, especially when the gel matrix is immiscible with silicone ink. This work presents a multi-axis ESP framework for fabricating volumetric silicone models with nearly solid infill and high surface quality. A field-based curved slicing strategy is introduced to preserve critical surface features and optimise layer height distribution, reducing height variation and ensuring model manufacturability. A boundary-conformal staggered toolpath algorithm further promotes uniform ink deposition, while adaptive toolpath width adjustment mitigates local overfilling and underfilling during curved printing. The framework is validated on a multi-axis robotic platform by fabricating wearable components, biomedical phantoms, and soft robotic structures. Characterization via surface scanning and X-ray CT confirms an infill ratio of 99.47% and a surface error below 1.5 mm (1% of the model size). The proposed framework greatly broadens the practical applications of ESP, enabling the fabrication of customised and functionally integrated soft devices.

ARTICLE HISTORY

Received 13 November 2025

Accepted 4 January 2026

KEYWORDS

Embedded silicone printing; multi-axis 3D printing; curved slicing; spatial toolpath generation; soft structure

1. Introduction

Silicone is a widely used soft material known for its excellent heat resistance, bio-compatibility, and electrical insulation properties [1]. With its outstanding durability, silicone is commonly employed in soft actuators that can safely interact with delicate objects and living tissues [2]. Its skin-like feel and biocompatibility also make silicone an ideal material for medical devices [3] and artificial tissues designed to replicate natural functions [4]. With growing requirements for functionality and personalisation in soft devices (e.g. the customised socket for low-limb prosthetics as shown in Figure 1), the fabrication of free-form silicone objects with complex geometries or topologies has become more critical and demanding. Nevertheless, conventional methods like mold-based casting struggle to produce such intricate designs due to their reliance on free-form multi-part molds [5], which lack the flexibility to adapt to other shapes for mass customisation.

Recent advancements in 3D printing have significantly expanded the possibilities for fabricating free-form silicone models [6]. A common approach is direct ink writing (DIW), where silicone is extruded and deposited following programmed paths. However, even with the development of in-situ curing [7], DIW generally struggles with large-scale models or intricate structures with long-span suspensions, as the low-stiffness of silicone material can lead to deformation and collapse under gravity. To address this, embedded silicone printing (ESP) has emerged as a promising solution. As illustrated in Figure 1, the ESP process extrudes silicone ink into a shear-thinning gel-like matrix, which stabilises the structure and prevents collapse during printing. With specially designed viscosity, the gel-based matrix allows the nozzle moves freely inside to deposit silicone layer by layer, and the matrix is removable or curable afterward [8].

CONTACT Guoxin Fang  guoxinfang@cuhk.edu.hk  Department of Mechanical and Automation Engineering, The Chinese University of Hong Kong, Shatin, New Territories, Hong Kong SAR, China; Institute of Intelligent Design and Manufacturing, The Chinese University of Hong Kong, Shatin, New Territories, Hong Kong SAR, China

© 2026 The Author(s). Published by Informa UK Limited, trading as Taylor & Francis Group

This is an Open Access article distributed under the terms of the Creative Commons Attribution License (<http://creativecommons.org/licenses/by/4.0/>), which permits unrestricted use, distribution, and reproduction in any medium, provided the original work is properly cited. The terms on which this article has been published allow the posting of the Accepted Manuscript in a repository by the author(s) or with their consent.

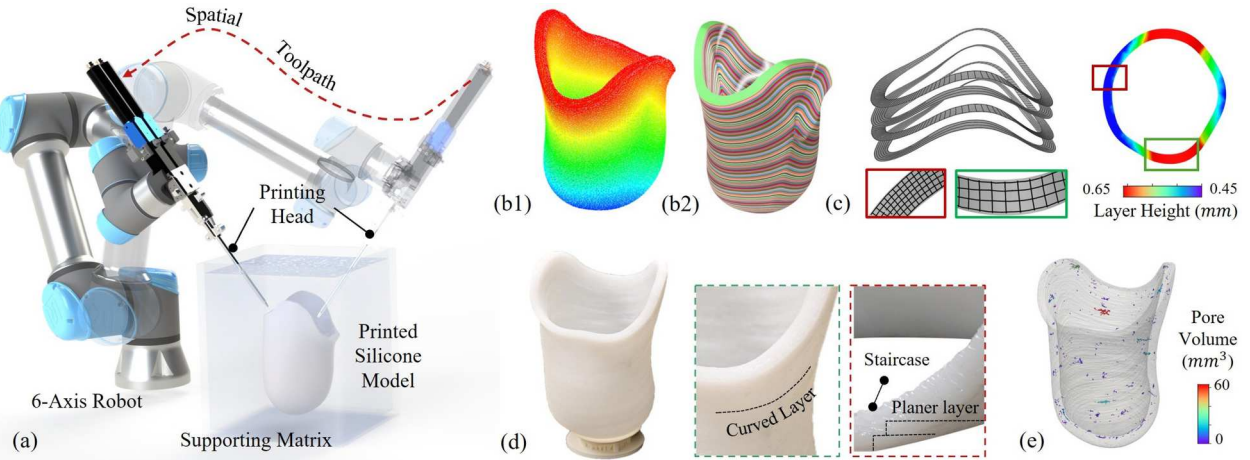


Figure 1. (a) Proposed multi-axis embedded silicone printing (ESP) system for fabricating free-form volumetric silicone models within a gel-like supporting matrix via robot-assisted spatial material deposition. The workflow of spatial toolpath generation includes (b) field-based slicing optimised for uniform layer height and subsequently, (c) boundary-conformal toolpath planning with in-layer staggered deposition. Here the toolpath density is controlled with extrusion constraint w.r.t., local layer height. (d) Compared with planar-based solution (printing result shown on the right), the proposed multi-axis ESP effectively reduces the staircase effect, enhancing surface finishing and geometric fidelity. (e) Fabrication results of a customised prosthetic socket with nearly solid infill (CT scan indicates infill ratio at 99.47%).

While the gel-based support makes ESP an effective solution for silicone printing with complex structures to avoid collapse [9], the immiscibility between silicone inks and the gel matrix inhibits filament fusion (details discussed in Section 3). Therefore, significant overlap between toolpaths is required to ensure adhesion, even with fine-tuned rheological properties (e.g. shear-thinning behaviour) of commonly used gel materials like Carbomer, leading to localised over-deposition of ink (as discussed in [10, 11] and also presented in Figure 3). For thin-shell models, the excess silicone can accumulate in surrounding directions without causing significant issues with the final product. However, for solid volumetric models, continuous ink accumulation causes significant geometry errors and can even distort the printed structure. As a result, the existing gel-based ESP process is generally limited to fabricating thin-wall structures or sparse infill models [11–13].

On the other hand, the usage of a support gel enables spatial alignment of silicone material through three-dimensional nozzle motion, which introduces greater design freedom and enhances fabrication flexibility. Especially for free-form models, employing a spatial toolpath can significantly enhance surface finishing quality by reducing the staircase effect (as highlighted in Figure 1(d)). Moreover, curved toolpaths can improve the continuity of material extrusion during ESP, mitigating issues such as stringing between discontinuous regions behaviour [14, 15] and the dimensional fidelity of printed models [16], its impact on deposition quality and material distribution has not been systematically studied. Consequently, strategies for spatial toolpath design and multi-

axis system integration that address these fabrication constraints in the ESP process are still lacking.

Here, we present a systematic study on multi-axis ESP for free-form volumetric models that extends the capabilities of gel-based ESP. In particular, we investigate the influence of nozzle orientation on printing quality in the multi-axis printing process. A comprehensive computational framework is developed to generate toolpaths that consider both design objectives and fabrication constraints in ESP for solid structures (as illustrated in Figure 1(b,c)). The framework integrates near-uniform-thickness curved slicing and width-constrained toolpath generation to address extrusion control challenges in free-form volumetric models. Additionally, the ink-volume control mechanism further improves printing quality by preventing excess material deposition, as demonstrated on a robot-assisted printing platform. The key contributions of this work are summarised as follows:

- Introducing multi-axis embedded silicone printing for free-form volumetric models, with solutions for spatial toolpath generation and printing direction optimisation to fabricate high-quality solid models.
- Investigating the influence of printing direction on print quality, effectively eliminating the staircase effect and maintaining printing continuity for multi-axis ESP.
- Developing a curved slicing strategy based on an iteratively optimised scalar field to preserve critical surfaces and ensure near-uniform layer heights.
- Proposing a width-constrained toolpath generation algorithm tailor-made for multi-axis ESP, which

- efficiently enables uniform material distribution and improves infill rates for complex models.
- Experimentally validating the proposed framework on a robot-assisted multi-axis ESP platform by fabricating various volumetric silicone models, including soft robotic components, biomedical phantoms, and customised wearable devices, demonstrating its practicality for rapid prototyping of functional soft systems.

To the best of our knowledge, this is the first work to achieve multi-axis volumetric ESP with both study in process optimisation and toolpath generation. The demonstrations reveal the potential applications in the rapid prototyping of soft robotics, medical devices, and tissue engineering.

2. Related work

Here we review the recent progress made on ESP and multi-axis 3D printing.

2.1. Embedded silicone printing

With the help of gel-based support, the development of embedded printing technology allows the fabrication of free-form soft objects such as soft robot pneumatic actuators [13]. Most existing studies on ESP focus on material and process development, emphasising the rheological and chemical properties of materials between the ink and support matrix to ensure successful printing. Notably, the effects of support matrix composition and rheology have been systematically examined in [17, 18], and various materials such as Carbopol [19], Laponite nanoclay [11], gelatin [20], and fumed silica nanoparticles [21] are further broadening the application scope of ESP. In this work, we adopt the widely used Carbopol support matrix with platinum-catalysed, silicone-based elastomer [8, 22] for physical validation, with detailed material characterisation presented in Section 3.

On the other hand, printing parameters and toolpath design significantly influence the quality of embedded printing [23]. Studies have thoroughly examined filament morphology under varying needle diameters, motion speeds, and extrusion pressures [11, 12]. For thin-shell structures, commercial planar-based slicers (e.g. Cura or Bambu Studio) are commonly used for toolpath generation. These studies offer valuable guidance for fine-tuning toolpath parameters such as line spacing [23]. However, less attention has been given to printing volumetric models with solid infill, where overlap between layers to ensure good material adhesion [12] can lead to over-extrusion (details also presented in

Section 3.2). While specialised curable support media [24–26] can help avoid such issues, they constrain material selection. In this work, we propose a general slicing and toolpath generation framework for solid ESP with precise extrusion control, applicable to both planar and spatial printing processes using general gel materials.

2.2. Multi-axis 3D printing and its application in ESP

Multi-axis 3D printing has garnered significant attention in recent years, as the ability to change the nozzle's orientation enables functionalities that surpass those of conventional planar-based printing [27, 28]. It has been integrated into various 3D printing processes, such as Digital Light Processing (DLP) to eliminate support structures and enhance surface quality [29, 30], Fused Filament Fabrication (FFF) to align filaments with stress tensors for model reinforcement [31], and Directed Energy Deposition (DED) to reduce deposition anisotropy and improve dimensional accuracy [32]. To date, multi-axis 3D printing has also been explored in diverse applications, including conformal electronics printing [33], food printing [34], and bioprinting of complex organs [35].

With the aid of a support matrix, ESP can naturally take great advantage of spatial material alignment. Existing studies have demonstrated the potential of ESP for printing 3D lattices [36] and vascular networks [37]. Additionally, with carefully designed spatial toolpaths, it has the great potential to improve surface finishing [38] and enhance extrusion continuity of ESP process (similar to spatial toolpath in DIW [39], whereas that method primarily targets parts with rotational features). On the other hand, although the toolpath is spatially optimised, its direct implementation on a conventional 3-axis ESP system remains challenging for achieving satisfactory printing performance. One key reason is that, in 3-axis ESP, the printing angle (see Figure 2(a)) varies due to the spatial nature of the toolpath and the fixed nozzle orientation. This variation adversely affects the overall printing quality of the ESP process. Sparman et al. [13] demonstrated that the nozzle orientation significantly affects filament position accuracy, while Arun et al. [15] showed that printing direction strongly impacts filament morphology of ESP. These findings highlight the critical role of orientation in ensuring consistent and high-quality deposition. In this work, we systematically study the relationship between the multi-axis printing process and filament morphology (Section 3.1), and conduct a solution of a robot-arm-based system to ensure good printing quality with controlled nozzle orientation.

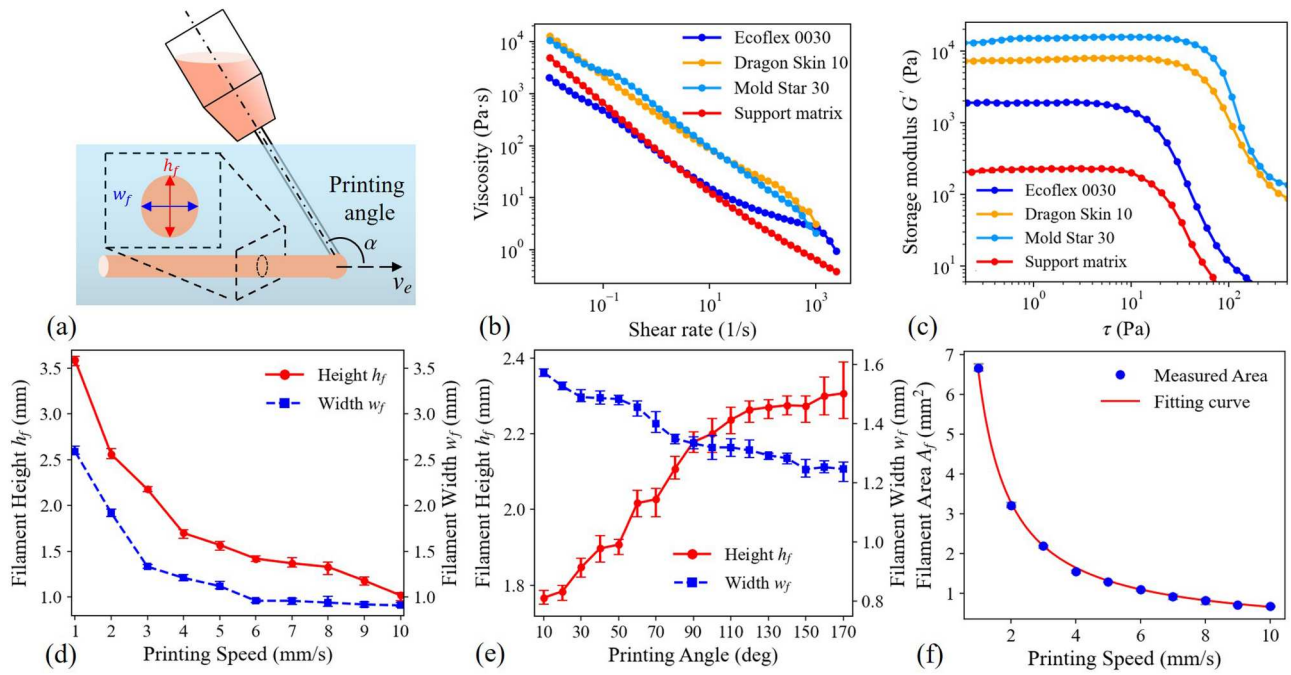


Figure 2. Analysis of rheological properties and filament morphology. (a) Illustration for filament dimension parameters and the printing angle. (b) Viscosity of ink and support matrix tested by rheometer (model: Haake Mars 40). (c) Storage modulus of ink and support matrix at the frequency of 1 Hz – both exhibit shear-thinning property. The storage modulus of ink is one to two orders of magnitude larger than the matrix material, which makes it ideal for ESP [17]. (d) Impact of the printing speed on filament morphology. (e) Impact of the printing angle on filament morphology (data tested under printing speed of 3 mm/s). (f) Variation of the cross-sectional area with printing speed, where polynomial fitting is used to fit the data for continuous calculation for extrusion constraint (Equation (2)).

Moreover, ESP differs fundamentally from conventional 3D printing processes (e.g. FFF or DLP) due to its unique filament morphology characteristics. Specifically, in ESP, the ratio between toolpath height and width dynamically changes with printing speed and is tightly interdependent with each other (reported in [12] and also demonstrated in Figure 2(d)). This dynamic behaviour makes it challenging to directly adapt existing multi-axis slicing methods designed for other processes, as they often assume fixed or predictable filament dimensions [40]. Consequently, these limitations restrict the flexibility and full potential of multi-axis ESP for complex geometries. Building on these insights, we propose a curved-layer slicing and width-constrained toolpath generation method (Section 4) to enable successful multi-axis ESP for free-form volumetric models. Case studies showcasing various applications are presented in Section 5.

3. Morphology and fabrication limits of multi-axis ESP

In this section, preliminary experiments on the filament morphology with multi-axis ESP are presented, detailing the materials used and the effects of printing speed and angle, concluding with toolpath design objectives and

fabrication constraints for the subsequent spatial printing toolpath generation.

3.1. Filament morphology with extrusion parameters

We first study the morphology of a single spatial path in multi-axis ESP where two primary printing parameters govern material deposition: the nozzle's moving speed v_e and the printing direction α (angle between the nozzle axis and the moving direction, see Figure 2(a)). These parameters directly influence the local deposition volume and material morphology. In our multi-axis ESP setup (Figure 1(a)), the extruder employs two servo motors to mix silicone components and maintain a constant extrusion speed, ensuring a steady material flow into the supporting gel over time. Consequently, adjusting v_e regulates the deposited volume locally, while varying α allows control over directional deposition behaviour.

The printing tests were conducted using Carbomer as the support bath and three silicone oils with different rheological properties as printing inks: Ecoflex 0030, Dragon Skin 10, and Mold Star 30,¹ with details provided in Section 5.2. The extrusion parameters (v_e and α) were varied along different printing path to investigate the

morphology of the printed silicone, which was characterised by the filament width w_f and height h_f of the cross-sections. As shown in Figure 2(d), at low printing speeds, the filament cross-sections were oval-shaped, with both w_f and h_f decreasing as the speed increased. At higher printing speed, the cross-sections became nearly circular due to larger yield areas in the support matrix, reducing confinement on the ink during extrusion [11]. These observations highlight the strong influence of printing speed on filament morphology. In multi-axis ESP, where local printing speeds vary dynamically to achieve spatially controlled extrusion, such morphological sensitivity becomes even more pronounced. To maintain relatively uniform layer geometry under these conditions, layer height (constrained with v_e) must be optimised in relation to the local printing-speed distribution and this is implemented by the algorithm described in Section 4.1.

We also observed that the printing angle had a significant influence on the morphology of the extruded silicone filament. As shown in Figure 2(e), when the nozzle orientation deviated from being perpendicular to the printing direction (i.e. $\alpha \neq 90^\circ$), both the filament width w_f and height h_f were markedly affected. Moreover, as previously reported in [13], the positional accuracy of the filament is reduced under non-perpendicular extrusion and requires compensation. In this study, to eliminate the influence of α on filament morphology and ensure precise deposition, we leveraged the multi-axis robotic setup to maintain perpendicular extrusion whenever possible. For regions with steep surface slopes or potential collision risks, the nozzle orientation is allowed to vary within $\alpha \in [70^\circ, 110^\circ]$ to minimise adverse effects (detailed in Section 5.2). Consequently, this approach enables more consistent control over filament morphology compared with conventional three-axis systems that employ a fixed nozzle orientation.

3.2. Objectives of toolpath design for volumetric ESP

Building on the investigation of single-filament morphology, we now present the following study to establish a suitable toolpath strategy for printing solid silicone structures, which can also be generalised to multi-axis ESP with dynamically changing printing speed. In printing solid models, three key aspects must be considered: ensuring sufficient fusion with the underlying filaments, achieving uniform ink spreading, and ensuring appropriate ink extrusion. To address these challenges, we employ a deliberate interlayer overlap to promote reliable bonding, a staggered toolpath

pattern to enhance ink uniformity, and a volume-preserving staggered strategy to mitigate over/under ink deposition.

For planar-based ESP printing of thin-walled models, the strategy for extrusion control and toolpath design is relatively straightforward: a constant printing speed can be applied to achieve $w_f \approx h_f$ (i.e. regular filament cross-section realised by high printing speeds) [11, 41]. Additionally, due to the immiscibility between silicone inks and the gel matrix, it is common to set the layer height H and toolpath width W smaller than the filament height h_f and width w_f , as expressed by $H = \beta \cdot h_f$ and $W = \beta \cdot w_f$ where $\beta < 1$ reflects the overlap ratio between filaments. Here, the selection of a smaller β indicates larger inter-path overlap and better filaments merging [12, 13]. However, this approach is not suitable for printing volumetric models. As illustrated in Figure 3(a,b) with the example of printing a solid cube, selecting a higher β results in poor inter-filament fusion, while a lower β (a strategy effective for thin-shell structures) causes severe over-extrusion and geometric distortion.

To address this limitation, we adopt a volume-preservation strategy, in which the toolpath width is intentionally set larger than the filament width to ensure consistent material deposition (illustrated in Figure 3(c, d)). Under this approach, W is determined by satisfying the constraint of volume preservation, where the total silicone volume V_{total} used for printing is calculated w.r.t., printing speed v_e and cross-section area A_f as:

$$V_{\text{total}} = \int_0^t v_e A_f(v_e) dt = C \cdot T_{\text{total}} \quad (1)$$

$$\approx \sum_{i=1}^N \| \mathbf{p}_i - \mathbf{p}_{i-1} \| \cdot H(\mathbf{p}) \cdot W(\mathbf{p}) \quad (\forall \mathbf{p}_i \in \mathcal{P}). \quad (2)$$

Here, Equation (1) quantifies the actual material extrusion governed by the extruder's capability, where T_{total} represents the total printing time. The parameter C denotes the unit extrusion volume per time step. It remains constant throughout the printing process, which is calibrated to be $6.57 \text{ mm}^3/\text{s}$. Equation (2) is the designed extrusion by toolpath parameter includes layer height $H(\mathbf{p})$ and toolpath width $W(\mathbf{p})$ at each waypoint. In this work, proper extrusion control is enabled for each time sequence (i.e. time $\Delta t = \| \mathbf{p}_i - \mathbf{p}_{i-1} \| / v_e(\mathbf{p})$, the time taken to move between two neighbouring waypoints), where we prioritise $H(\mathbf{p})$ to be first computed by curve-layer decomposition of the printed model (see details in Section 4.1) and the volume-preserving ensures:

$$C \cdot \frac{\| \mathbf{p}_i - \mathbf{p}_{i-1} \|}{v_e(\mathbf{p})} = \| \mathbf{p}_i - \mathbf{p}_{i-1} \| \cdot H(\mathbf{p}) \cdot W(\mathbf{p}) \quad (3)$$

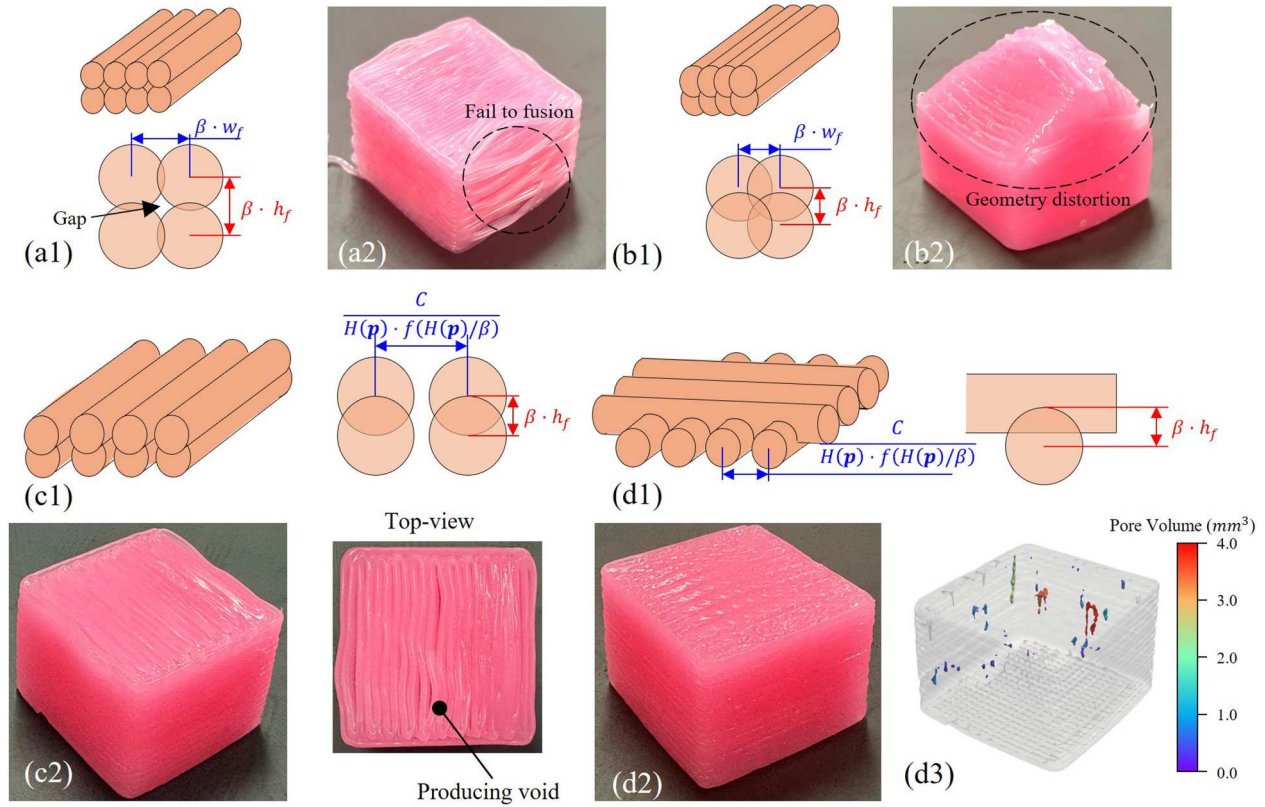


Figure 3. Printing results of a solid cube fabricated under different toolpath generation strategies. (a) A toolpath with minor overlap (e.g. large $\beta = 0.9$) in both width and height leads to insufficient fusion due to immiscibility between silicones and matrix materials. (b) In contrast, a large overlap (small $\beta = 0.5$) causes over-extrusion and results in geometric distortion. (c) A non-staggered toolpath with large inter-layer overlap and a volume-preserving width constraint enables stable extrusion, but produces vertically aligned voids due to the repetitive stacking direction. (d) When both the volume-preserving constraint and the staggered-toolpath strategy are applied, a dense and uniform structure is achieved, effectively minimising internal pores and geometric deviation.

In this way, the designed proper toolpath width $W(\mathbf{p})$ for waypoint \mathbf{p} is constrained to

$$W(\mathbf{p}) = \frac{\mathcal{C}}{H(\mathbf{p}) \cdot v_e(\mathbf{p})} = \frac{\mathcal{C}}{H(\mathbf{p}) \cdot f(H(\mathbf{p})/\beta)}. \quad (4)$$

which is determined by the local layer height. Here, $f(\cdot)$ is a function calibrated from physical data presented in Figure 2(d), representing the relationship between printing speed and the morphology of the filament cross-section. When choosing local printing speed for multi-axis ESP by $v_e(\mathbf{p}) = f(h_f(\mathbf{p})) = f(H(\mathbf{p})/\beta)$, we need first to determine the parameter β . Although a smaller β means better interlayer fusion and improved surface quality [13], it also results in sparser in-layer toolpath (as described in Equation (4)), which increases the risk of entrapping the supporting matrix and forming larger infill defects. Considering the trade-offs between surface quality and infill performance, we selected $\beta = 0.5$ for all experiments as filaments printed at different velocities merged reliably under this condition while also maintaining good infill quality (the result can be found in Section 5.3).

With the toolpath-width constraint, the extrusion compensates for the 'gap' regions between adjacent filaments by slightly over-extruding in height, ensuring that the total extruded volume aligns with the design requirements. As illustrated in Figure 3(c), although this compensation improves inter-layer bonding and prevents over-extrusion, uniformity remains limited when successive layers shared the same toolpath direction, resulting in the formation of vertical voids along the stacking direction. To overcome this limitation, a staggered toolpath strategy is employed, in which the printing direction of each successive layer is arranged perpendicular to that of the previous one, as shown in Figure 3(d). This interlaced deposition pattern significantly reduced internal pores, as confirmed by the CT analysis, which revealed a pore ratio of 0.1% of the total volume.

It is worth mentioning that the proposed volume-preservation and staggered-toolpath strategies can be generalised to multi-axis printing scenarios with variable printing speeds or non-uniform extrusion rates, and the objectives for toolpath design contain:

- With computed variable layer height, local toolpath width needs to be constrained (computed by Equation (4)) at each waypoint to ensure adequate infill.
- The toolpath between neighbouring curved layers should stagger with each other to ensure proper fusion;

Existing algorithms for spatial toolpath generation do not account for these requirements in embedded printing. In the following section, we present a computational framework specifically designed for toolpath generation in multi-axis ESP of volumetric models.

4. Width-constrained spatial toolpath for multi-axis ESP

With a given volumetric model with free-form surfaces (represented as a tetrahedral mesh \mathcal{M}), our computational pipeline starts from generating a set of curved working surfaces $\{\mathcal{S}_k\}_{k=1,2,\dots,N}$ to decompose \mathcal{M} . As illustrated in Figure 4, these curved printing layers define the local layer thickness, which is controlled within the capability of the physical extruder setup (as discussed in Section 3). In the framework and as previously discussed, the critical region is preserved to ensure the best printing quality and the continuity of the print (e.g. top curved surface of the prosthetic socket model highlighted in green on Figure 4(b-d)).

Subsequently, the spatial toolpath \mathcal{T} (discretized as a set of waypoints \mathcal{P}) is computed for each curved working surface, taking into account width constraints. Specifically, as discussed in Section 3.2, crossing-based toolpaths with two different patterns (contour-parallel and staggered zig-zag pattern) are employed to ensure proper infill during the ESP process.

In the following, we first demonstrate the method to optimise for layer height with iterative-based optimisation, then present the technique of width-constraint toolpath computing.

4.1. Iteration-based curved slicing with layer height control

To compute curved working surfaces for multi-axis ESP, we follow a field-based computing strategy [42], in which a scalar field \mathcal{G} is defined and each vertex of the model is assigned a scalar value $g(\mathbf{x})$. The field \mathcal{G} is then optimised, and the curved layers are extracted as iso-surfaces of the input model, expressed as $\mathcal{S} = \mathbf{x} | \forall \mathbf{x} \in \mathbb{R}^3, g(\mathbf{x}) = c$, where c is the iso-value and \mathcal{S} is represented by a triangular mesh. Note that the material accumulation direction in this way is controlled by the gradient of \mathcal{G} , which is installed at the center of

each element $\nabla g(e)$. The local layer height is also defined as the norm of this gradient, i.e. $H(e) = \|\nabla g(e)\|$.

With the need to protect surface quality and ensure that the printing angle α and layer height H do not exceed the capability of the printing setup, as discussed in Section 3, we encode the objective of (i) critical-surface preservation, (ii) target layer height, and (iii) printing direction smoothness via:

$$\begin{aligned} \arg \min_{\mathcal{G}} \quad & \omega_a \sum_{\mathbf{x} \in \Omega} \|g(\mathbf{x}) - \bar{G}_\Omega\|^2 + \omega_l \sum_{e \in \mathcal{M}} (\|\nabla g(e)\| - H_t)^2 \\ & + \omega_h \sum_{f \in \mathcal{M}, e_i \cap e_j = f} \|\nabla g(e_i) - \nabla g(e_j)\|^2, \end{aligned} \quad (5)$$

where the first term preserves the surface quality of the critical region Ω and ensures continuous printing, with \bar{G}_Ω representing the average guidance value of Ω . The second term optimises for layer height with the target H_t set to the unit height for numerical computation, while the third term evaluates gradient compatibility (w.r.t. printing direction). Here, e_i and e_j are neighbouring elements that share the same face f ; optimising gradient compatibility prevents the formation of highly curved surfaces that require large local printing angles. ω_a , ω_l , and ω_h are corresponding weighting for each objective.

However, directly solving the optimisation in Equation (5) by gradient-based optimisation will lead to a local minimum solution as the layer thickness objective contains a nonlinear evaluation of $\|\nabla g\|$. Additionally, \bar{G}_Ω is also an unknown variable in the first place in the optimisation [42]. As a result, the layer height cannot be controlled within a small range to satisfies extrusion ability (see the illustration in Figure 4(e) iteration 1).

Tackling this issue, and considering the objectives in Equation (5) are mostly related with ∇g , which naturally formulates a gradient vector field, we adopt an iterative optimisation approach with vector-scalar field converting to find a better solution for curve layer slicing. As demonstrated in Figure 4(b,c), each element has been assigned with vector $\mathbf{v}(e)$, which formulates a vector field, and the optimisation problem in Equation (5) can be convert into find an optimal vector field as

$$\begin{aligned} \arg \min_{\mathbf{v}} \quad & \omega_l \sum_{e \in \mathcal{M}} \left\| \mathbf{v}(e) - \frac{\nabla g(e)}{\|\nabla g(e)\|} \right\|^2 \\ & + \omega_h \sum_{f \in \mathcal{M}, e_i \cap e_j = f} \|\mathbf{v}(e_i) - \mathbf{v}(e_j)\|^2 \\ \text{s.t.} \quad & \mathbf{v}(e) = \mathbf{n}_f(e) \quad (\forall e \in \Omega) \end{aligned} \quad (6)$$

where the layer height objective is enforced by setting the initial vector close to the normalised gradient (i.e. to achieve uniform layer height). Additionally, critical region protection is formulated as a Neumann boundary

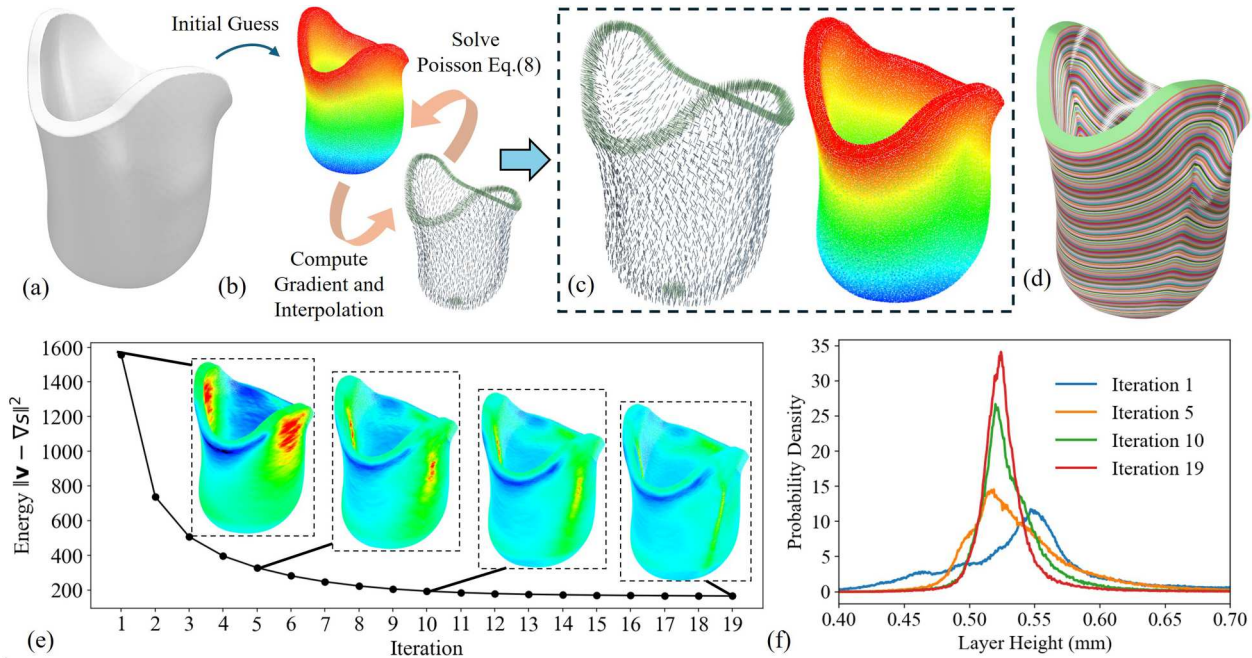


Figure 4. Diagram for showing the pipeline of our field-based curved slicing method. (a) Input Solid model \mathcal{T} for slicing. (b) The process of scalar field optimisation. Left top: initially computed scalar field; Right bottom: update vector field by solving Equation (6), the green vectors highlight user-defined anchor vectors in critical regions and cyan vectors are obtained via interpolation. (c) The final gradient field and scalar field lead to optimised layer height variation. (d) The curved working surfaces are extracted as a set of iso-surfaces. (e) Error convergence of the objective function $\mathcal{O}_{\text{align}}$ in Equation (7) w.r.t., iteration count, which is well reflected in (f) the layer-height distribution after different numbers of iterations. The results show that the layer height is effectively controlled, ensuring improved extrusion stability in the ESP process.

condition in the constraints, ensuring that in these regions, the material growth direction aligns with the normal \mathbf{n}_f of the boundary face f . All objectives in Equation (6) are quadratic, so a linear system can be used to directly find the optimal vector field \mathcal{V} , and the corresponding scalar field can then be computed by minimising

$$\begin{aligned} \arg \min_{\mathcal{G}} \quad & \mathcal{O}_{\text{align}}(\mathcal{G}, \mathcal{V}) = \sum_{e \in \mathcal{M}} \|\nabla g(e) - \mathbf{v}(e)\|^2, \\ \text{s.t. } & g(\mathbf{x}) = \bar{g}_\Omega \quad (\forall \mathbf{x} \in \Omega) \end{aligned} \quad (7)$$

which is equivalent to solving the Poisson's equation (also a linear system) [43] as

$$\Delta \mathcal{G} = \nabla \cdot \mathcal{V} \quad (8)$$

Here Δ is the Laplacian operator, and the right side computes the divergence of the vector field. Experimentally, $\mathcal{O}_{\text{align}}$ also implicitly reflects the variation of layer height (refer to Ref. [43] and Figure 4(e)), and we invite an iteration-based process to find a smooth scalar field with controlled distribution of layer height by the following steps:

- Step 1: compute initial scalar field \mathcal{G}_0 by solving Equation (5).
- Step 2: take \mathcal{G}_0 as input and find optimised vector field \mathcal{V} that satisfies fabrication objectives defines in Equation (6).

- Step 3: compute the Poisson's equation Equation (8) to find corresponding \mathcal{G}_{new} , evaluate $\mathcal{O}_{\text{align}}(\mathcal{G}_{\text{new}}, \mathcal{V})$ with Equation (7).

Steps 2 and 3 are run iteratively by taking $\mathcal{G}_{\text{new}} = \mathcal{G}_0$ back into step 2 at each iteration. The iteration terminates when $\mathcal{O}_{\text{align}}$ is converge (i.e. change less than 10^{-2} times last iteration). It is worth noting that, due to the boundary protection requirement (i.e. Neumann boundary in Equation (6)), it is mathematically proven that the field cannot be optimised into a unit field with constant layer height everywhere. However, using the iteration-based solver introduced in this work, the layer height is optimised to be as uniform as possible, as shown in Figure 4(f). For each vertex on the printing surface, the layer height $H(x)$ is computed from the final gradient length of the scalar field, which serves as input for the width-constrained toolpath optimisation to determine $W(\mathbf{p})$.

4.2. Width-constrained toolpath design with staggered pattern

With the curved printing layers generated (Section 4.1), the next step is to develop a toolpath generation algorithm on each individual layer. As previously discussed, generating toolpaths for multi-axis ESP to achieve

good extrusion in volumetric models requires addressing two key objectives: (1) toolpaths are to be staggered between layers to fill gap regions effectively, and (2) local toolpath width must be controlled based on the defined $W(\mathbf{p})$, which is computed from the layer height.

Here, we present a solution that employs a staggered pattern combining boundary-conformal and perpendicular zig-zag patterns. We first demonstrate this approach on a printing layer with uniform layer height, where both patterns are controlled by frequency parameters to ensure an equally spaced stripe arrangement. Subsequently, a deformation-driven parameterisation method is introduced to incorporate non-uniform layer heights as a scalar field \mathcal{H} into the toolpath generation, ensuring all fabrication requirements are met.

As demonstrated in Figure 5, for all the printing layer $\{\mathcal{S}\}$ generated as iso-layer of \mathcal{M} , the pattern is defined by the index. For even layers, the nozzle moves along the contour shape to form a boundary-conformal pattern, while in odd layers, the nozzle's movement trajectory is orthogonal to the contour shape. This approach ensures a more uniform distribution of ink in both the circumferential and radial directions, even within iso-layers with complex geometry (more result can be seen in the result Section 5).

Without the loss of generality, we first present our toolpath computing algorithm on a curved surface with a constant toolpath width W . For boundary-conformal pattern, we follow field-based strategy where the computation starts with the generation of a geodesic distance field using the boundary as source [44] (see Figure 5(b,c)). With computed distance as a scalar field \mathcal{D} , each vertex of $\mathbf{x} \in \mathcal{S}$ is assigned with a scalar value $d(\mathbf{x})$ and the k -th toolpaths \mathcal{L}^k on the even layer can

be generated by extract from \mathcal{S} as iso-contour

$$\mathcal{L}_{\text{even}} = \{\mathcal{L}_{\text{even}}^k\} = \{\mathbf{p} \mid \forall \mathbf{p} \in \mathbb{R}^3, d(\mathbf{p}) = \tau \cdot kW, k \in \mathbb{Z}^+\}. \quad (9)$$

Since \mathcal{D} is a geodesic distance field, a constant width of W can be maintained between neighbouring toolpaths. The factor τ (ranging from 0.98 to 1.02 based on our tests) is introduced to adjust the total length computed in Equation (9), ensuring it matches the required material volume for silicone (computed by Equation (1)).

On the other hand, computing odd layers with an orthogonal pattern to the boundary-conformal toolpath is non-trivial. Mathematically, there is no guarantee of finding another scalar field $\phi(\mathbf{x})$ such that its gradient is perpendicular to $\nabla d(\mathbf{x})$ everywhere in the mesh while keeping a constant toolpath width. Specifically, the toolpath objectives of staggering and width constraint, expressed as $\nabla \phi(\mathbf{x}) \cdot \nabla d(\mathbf{x}) = 0$ and $|\nabla \phi(\mathbf{x})| = c$ ($\forall \mathbf{x} \in \mathcal{S}$), respectively, may conflict with each other in layers with complex geometries.

We propose a periodic scalar field with frequency control to address the challenge of generating toolpaths within a width constraint. As shown in Figure 5(d), at each vertex the periodic scalar valued is defined w.r.t., complex-number form as

$$\Psi(\mathbf{x}) = e^{i\psi(\mathbf{x})} = \cos(\psi(\mathbf{x})) + i \sin(\psi(\mathbf{x})), \quad (10)$$

where $\psi(\mathbf{x})$ is the angle (or phase) at the vertex as another parameterisation of the periodic scalar field. With this periodic scalar field, the printing toolpath is extracted with initial phrase, and the toolpath width is controlled by the frequency (w.r.t., the phase change $\nabla \psi$). In this way, the objective of toolpath generation

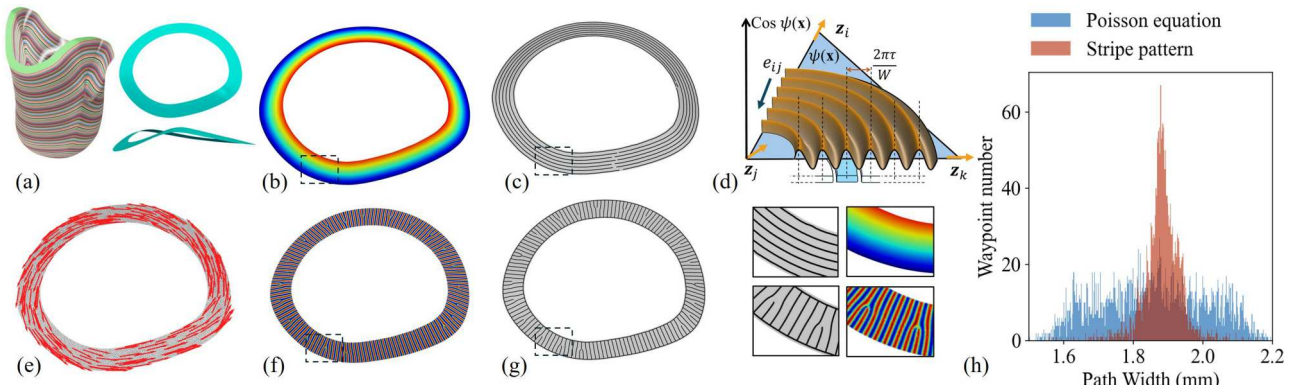


Figure 5. An overview of our algorithm for boundary-conformal staggered toolpath generation. (a) Curved Printing layer. (b) Boundary conformal toolpath computed for odd layer. (c) Boundary conformal toolpath computed for even layer. (d) Illustration of toolpath generation using a periodic function on a triangle element. (e) Control vector field $\mathbf{z}(\mathbf{x})$. (f) The periodic scalar field ψ , which gradient $\nabla \psi$ perpendicular with $\mathbf{z}(\mathbf{x})$. (g) the stripe pattern toolpath generated for even layers. (h) Comparison on toolpath widths distribution generated by different methods.

with scalar field computing is formulated as

$$\begin{aligned} \arg \min_{\Psi} \quad & \mathcal{O}_{\text{phrase}} = \sum_{\forall \mathcal{E}_{ij} \in \mathcal{S}} \|\Psi_j - e^{i\Delta\psi_{ij}}\Psi_i\|^2 \\ \text{s.t.} \quad & \Delta\psi_{ij} \equiv \tau \cdot \frac{2\pi}{W} \cdot \frac{1}{2} (\langle \mathbf{z}_i, \mathbf{e}_{ij} \rangle + \langle \mathbf{z}_j, \mathbf{e}_{ij} \rangle) \\ & (\forall \mathcal{E}_{ij} \in \mathcal{S}). \end{aligned} \quad (11)$$

Here in the constraint, the vector $\mathbf{z}(\mathbf{x}) = (\nabla d(\mathbf{x}) / \|\nabla d(\mathbf{x})\|)^\perp$ presents the normalised gradient rotated by 90 degree (denoted as \perp), which both enforces the orthogonality condition and ensures uniform toolpath width, as the gradient of the scalar field is aligned with the rotated gradient of the distance field, and to have constant norm. The target phrase change $\Delta\psi_{ij}$ between vertex \mathbf{v}_i to \mathbf{v}_j along the edge \mathcal{E}_{ij} is computed by projection with dot product $\langle \cdot, \cdot \rangle$. The constrained optimisation Equation (11) is in a quadratic form and can be effectively solved by a linear system with conversion from the complex variable into real-valued vectors (details can be found in [45]).

With the optimised periodic field, the printing path for odd layer is extracted as crest lines of the periodic function (see Figure 5(d)), which can be written as

$$\mathcal{L}_{\text{odd}} = \{\mathbf{p} \mid \forall \mathbf{p} \in \mathbb{R}^3, \psi(\mathbf{p}) = 2N\pi, N \in \mathbb{Z}\}. \quad (12)$$

Note that the frequency is controlled by the variable $\frac{\tau}{W}$ and is determined iteratively using a binary search method to match the required material volume. Both toolpath $\mathcal{L}_{\text{even}}$ and \mathcal{L}_{odd} are then connected into a continuous path using the A* (shortest-path-search) algorithm [46]. As illustrated in Figures 5(h) and 8(c), compared with the real-number-based toolpath with $\phi(\mathbf{x})$ obtained using the Poisson-equation solver (similar to Equation (8) – matching $\Delta\phi = \nabla \cdot \mathbf{z}$), the stripe-like pattern proposed in our framework significantly optimises the path width to better match the target value, thereby improving extrusion quality.

4.3. Spatial toolpath generation with variable-width control

This subsection focuses on computing the final physical printing parameters for multi-axis ESP, considering volume preservation in the printing case with variable layer height $H(\mathbf{x})$ where corresponding changes on toolpath width $W(\mathbf{x})$ (computed with Equation (4)) are necessary to ensure consistent material deposition. This is computationally infeasible to be directly enforced in the aforementioned constant-width-based toolpath generation method.

Here, we propose a deformation-driven method to solve this fabrication constraint. As illustrated in Figure 6, the original printing surface \mathcal{S} is first mapped

into a deformed shape \mathcal{S}^d . The purpose of this deformation-based mapping is to enforce a uniform target toolpath width on \mathcal{S}^d (i.e. $W(\mathbf{x})$ is a constant everywhere in the surface). This allows the methods described in Equations (9) and (12) to be directly applied to \mathcal{S}^d , with the final printing toolpath computed with inverse mapping to the original surface, naturally satisfying the original width requirements. The deformation-driven mapping is determined by solving the following optimisation problem:

$$\arg \min_{\mathcal{S}^d = \{\mathbf{V}_f^d\}} \mathcal{O}_{\text{map}} = \sum_{\forall f \in \mathcal{S}} \|\mathbf{N} \cdot \mathbf{V}_f^d - \mathbf{R}_f \cdot \mathbf{S}_f \cdot (\mathbf{N} \cdot \mathbf{V}_f)\|_F^2. \quad (13)$$

Here f represents a triangular element of the surface, with its vertices position $\mathbf{x}_i = [x_i, y_i, z_i]$ organised into the matrix $\mathbf{V}_f = [\mathbf{x}_1, \mathbf{x}_2, \mathbf{x}_3]^T \in \mathbb{R}^{3 \times 3}$. The scaling matrix, $\mathbf{S}_f = \text{diag}(s_f, s_f, s_f)$, encodes the local scaling factor s_f which adjusts the width to match the target value. The scaling factor is computed as:

$$s_f = \frac{3\bar{W}(\mathcal{S})}{\sum_{i=1}^3 W(\mathbf{x}_i)} \quad (14)$$

where $W(\mathbf{x}_i)$ is the target toolpath width at vertex \mathbf{x}_i , and the term $\bar{W}(\mathcal{S})$ represents the average toolpath width over the entire surface. The translation matrix $\mathbf{N} = \mathbf{I}_{3 \times 3} - \frac{1}{3}\mathbf{1}_{3 \times 3}$ ensures evaluations are translation-invariant, while the rotation matrix \mathbf{R}_f eliminates the effect of affine transformations. The optimisation in Equation (13) solves for both deformed vertex positions \mathbf{V}_f^d and \mathbf{R}_f using a local-global solver, which converges efficiently in a few iterations [47].

The field-based width-constrained toolpath generation method is then applied in \mathcal{S}^d , where Equations (9) and (12) define toolpath and are discretised into waypoints $\{\mathbf{p}^d\}$, ensuring the local width $W(\mathbf{p}^d)$ remains constant. For each waypoint \mathbf{p}^d , the barycentric coordinates $(\gamma_1, \gamma_2, \gamma_3)$ are computed with respect to the corresponding triangle $f \in \mathcal{S}^d$ as:

$$\begin{aligned} \gamma_1 &= \frac{\mathcal{A}(\mathbf{p}, \mathbf{x}_2^d, \mathbf{x}_3^d)}{\mathcal{A}(f)}, \quad \gamma_2 = \frac{\mathcal{A}(\mathbf{p}, \mathbf{x}_1^d, \mathbf{x}_3^d)}{\mathcal{A}(f)}, \\ \gamma_3 &= 1 - \gamma_1 - \gamma_2 \end{aligned} \quad (15)$$

where $\mathcal{A}(\cdot)$ evaluates the area of a given triangle.

The final waypoint \mathbf{p} used in multi-axis ESP, which contains both positional and directional information, is mapped from the offset surface \mathcal{S}^d back onto the original surface \mathcal{S} using the computed barycentric coordinates:

$$\mathbf{p} = [\gamma_1 \mathbf{x}_1 + \gamma_2 \mathbf{x}_2 + \gamma_3 \mathbf{x}_3, \vec{\mathbf{n}}_f] \in \mathbb{R}^6 \quad (16)$$

where $\mathbf{x}_i \in \mathcal{S}$ denotes the vertex positions of the corresponding triangle on the original surface. As shown in

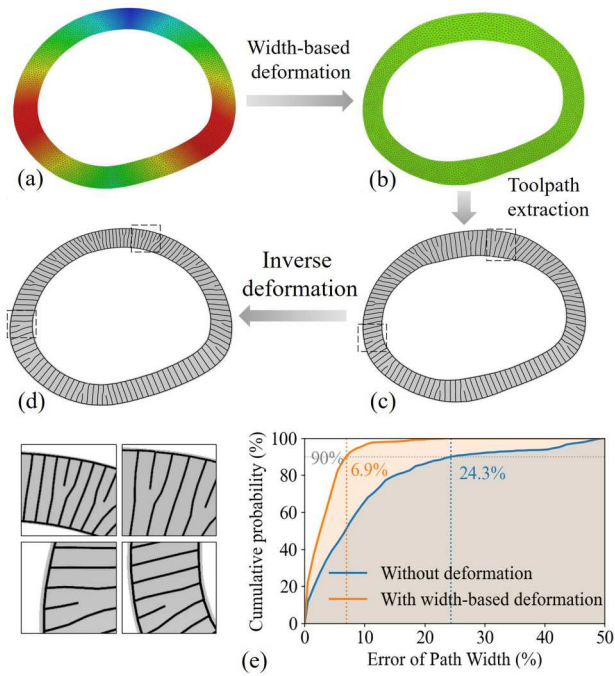


Figure 6. An overview of our width-constrained toolpath algorithm (a) Original isolayer with path-width field. (b) Isolayer after width-based deformation with constant path-width field. (c) Equal-width toolpath generated on deformed isolayer(d) Width-constrained toolpath extracted on original isolayer. (e) Cumulative distribution of path-width error with and without width-based deformation.

Figure 6(e), with the help of this mapping-based approach, the precision of the toolpath width has been significantly improved and the error required to achieve 90% cumulative probability reduced from 24.3% to 6.9%. It is worth mentioning that the local printing direction \vec{n}_f is assigned as the unit normal of the face $f \in \mathcal{S}$ to always keep local printing angle $\alpha = 90^\circ$, ensuring smooth orientation transitions and geometric consistency in the printing process.

5. Result and discussion

We evaluated the performance of the proposed toolpath generation framework for multi-axis ESP on various volumetric models, including applications in soft robotics, medical phantoms, and wearable devices. This section provides a detailed description of the robot-assisted ESP setup, along with both computational and experimental fabrication results. Additional details can also be found in the supplemental video.²

5.1. Computational details and test cases

The computational framework, including curved slicing with optimised layer height (Section 4.1) and width-

constrained spatial toolpath generation (Section 4.2), was implemented in C++ using Visual Studio. High-quality isotropic tetrahedral meshes, required as input for the computation, were generated using a particle-based method [49]. All linear equation solvers and matrix computations were accelerated with the Eigen library [50].

With the ability to handle volumetric models with arbitrary internal geometry, the first test case of the proposed ESP method is pneumatic-driven soft robots. As shown in Figure 7(a), these robots are designed with various internal structures (e.g. placement of solid regions highlighted in yellow), enabling them to deform into different shapes. Conventional modelling is challenging to fabricate these design due to irregular internal channels requiring complex, hard-to-remove molds. Existing ESP solutions proposed for thin-wall structures [11, 41] also cannot handle these models, as large overlaps in x-y and z directions cause geometry distortion when printing solid regions (as previously discussed in Section 3.1). Our toolpath generation overcomes this by using staggered toolpath with boundary-conformal and zig-zag patterns for odd and even layers, respectively, ensuring geometry adaptation of toolpath, width-constrained toolpath distribution, and robust filament fusion (see Figure 7(c)). This achieves precise extrusion control for leak-free fabrication (see Figure 11 and Section 5.3 for results). Notably, our slicing algorithm presented in Section 4.1 degenerates into a planar-based one for this case, with critical surfaces Ω selected as the top and bottom layers and generating a constant scalar field gradient $\nabla g = [0, 0, 1]$ throughout the model (Figure 7(b)).

The second model tested is a vascular phantom with obstructive solid regions. As shown in Figure 8(a), the aortic atheroma is located on the inner curvature of the aortic arch and the proximal descending aorta, areas with a high clinical incidence of atherosclerosis due to hemodynamic properties (highlighted in purple). This model combines both thin-shell and solid regions, with five critical regions selected as boundary conditions for protection, which present challenges that existing methods designed for thin-wall structures [8, 51] are unable to address. The slicing result and toolpath for the critical curved working surface using the proposed method are shown in Figure 8(b,d), respectively. Compared to planar-based slicing, multi-axis printing significantly ensures continuous extrusion, as highlighted in the zoom-in view of the aortic atheroma region (near Ω_3). Quantitatively, our iteration-based curved-layer slicing method yields more uniform layer heights, with their variation reduced by approximately

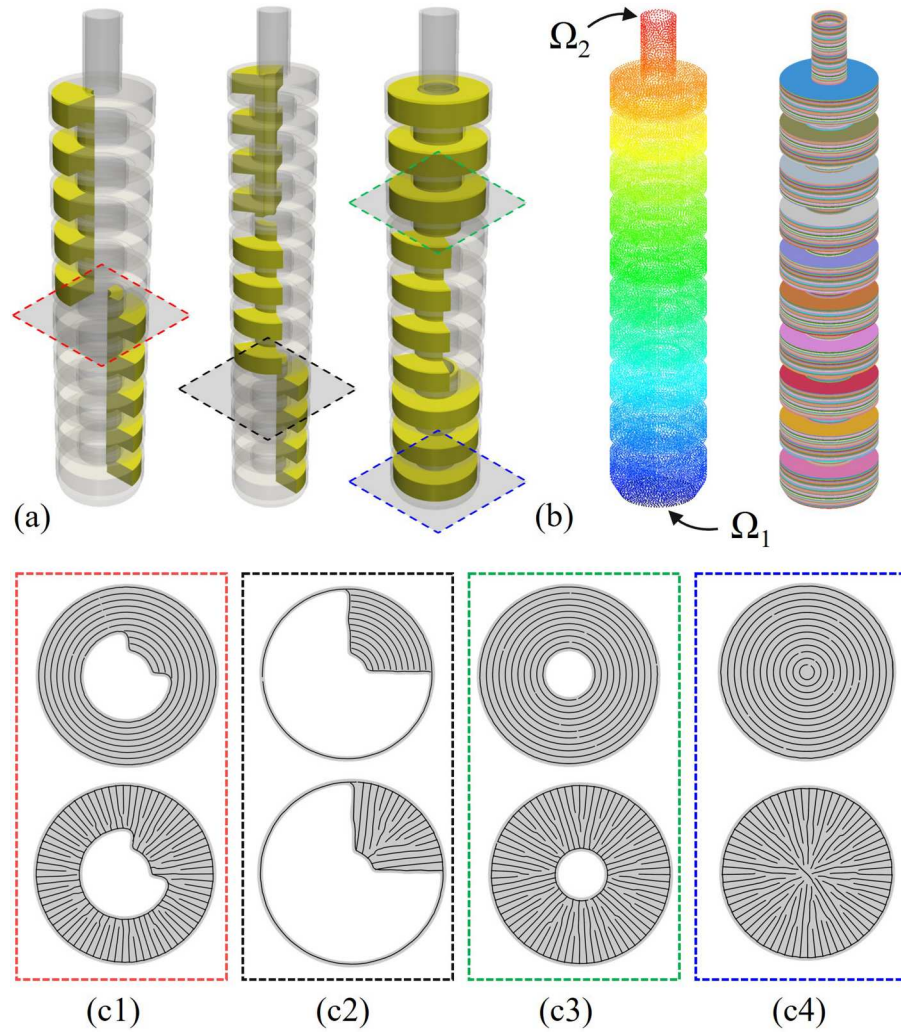


Figure 7. (a) Computational results for three soft robot models with various solid internal cavities (solid regions shown in yellow, with thin-wall parts rendered in semi-transparent gray). (b) With the top and bottom layers selected as the ROI, constant layer heights are generated, and the planar surfaces are computed. (c) Toolpath generation for various layers: odd layers use boundary-conformal patterns, and even layers use perpendicular zig-zag patterns, both optimised for leak-free soft robot fabrication via ESP.

70% compared with that computed using harmonic constraint [42], as shown in Figure 8(c).

We further evaluated the performance of our toolpath algorithm on a model with free-form volumetric parts and an integrated internal cavity, as shown in Figure 9. The deformable membrane consists of two parts (base and top membrane), and can be actuated pneumatically to mimic various human body shapes [52]. Conventional molding methods for such designs are time-consuming and can fail to ensure airtightness due to the gluing between parts [48]. In contrast, multi-axis ESP allows it to be fabricated in one piece with the optimised spatial toolpath, where the base and top region with variable thickness are fabricated together with an overlapping interface (as shown in Figure 9(b)), ensuring robust interfacial bonding and air-tightness. As can be seen from Figure 9(c), our

iteration-based curved-layer slicing with surface-preserving capability maintains extrusion continuity on critical surfaces (denoted as $\Omega_1 - \Omega_4$). The computed boundary-conformal and perpendicular zig-zag toolpath is illustrated in Figure 9(d), demonstrating the effectiveness of our deformation-driven variable-width control algorithm (presented in Section 4.3). Without width control, large variations in layer height result in over- and under-deposition (Figure 9(e), left). Our algorithm distributes ink effectively across the curved surface, ensuring that approximately 90 % waypoints are well adjusted according to layer height (Figure 9(f)), reducing extrusion errors by 82%.

The final model is a customised lower-limb prosthetic socket (see Figure 1), with its shape captured via CT scan and designed to perfectly fit the patient [53]. The conventional mold-based fabrication method is expensive

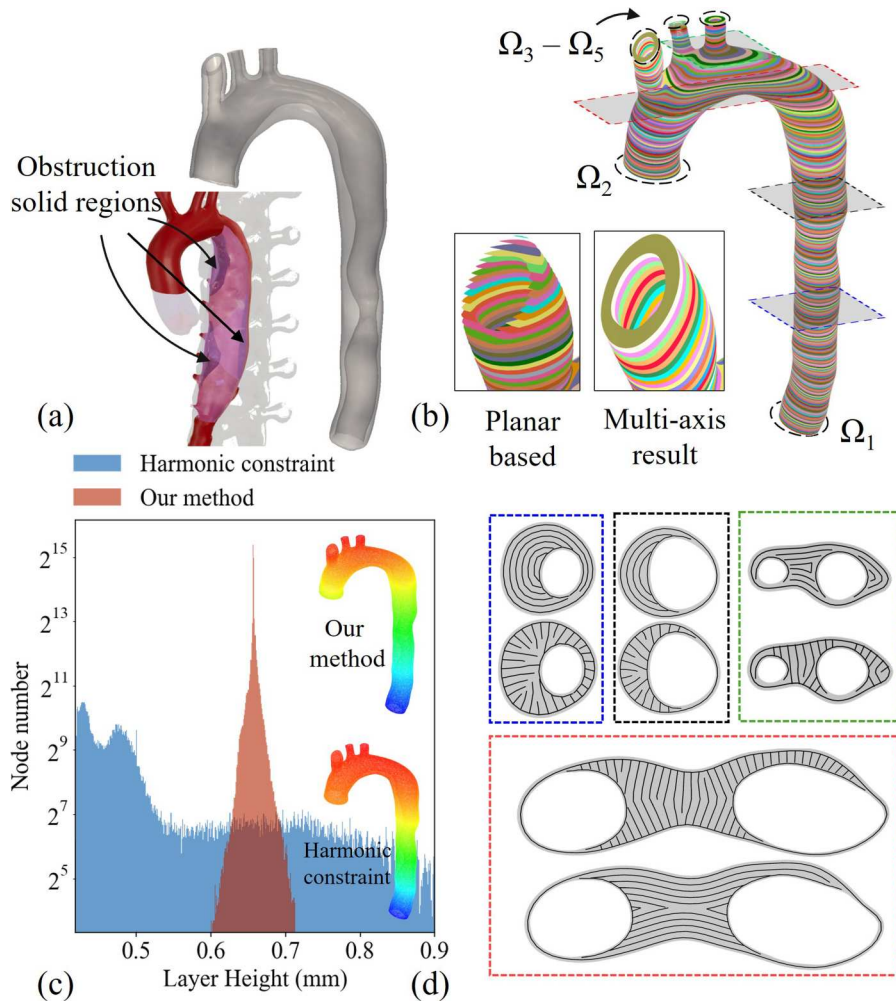


Figure 8. (a) Computational results of the customised vascular phantom containing both thin-shell and solid regions. (b) Compared with the planar-based solution, the multi-axis ESP approach preserves the geometric fidelity and printing quality of critical regions through the computation of curved layers. (c) Our iterative curved-slicing algorithm effectively controls the distribution of layer height, ensuring better material deposition and smooth surface transitions. (d) Staggered toolpaths computed on odd and even layers ensure stable extrusion and leak-free solid printing.

and labour-intensive, making rapid, low-cost personal customisation difficult. Furthermore, existing planar-based ESP cannot ensure continuous material extrusion, resulting in poor surface finishing on highly curved regions (highlighted in the zoom-in view of Figure 1(d)). As previously discussed, our curve-layer slicing and spatial toolpath design for ESP demonstrates superior computational results. Through iterative processing, the variation in layer height is reduced by 60% (the standard deviation decreases from 0.0852 mm to 0.0327 mm), as shown in Figure 4. Meanwhile, the deformation-based algorithm ensures that 95% of spatial waypoints are precisely controlled, achieving consistent extrusion and substantially improving performance compared with direct computation (see Figure 6).

Notably, the proposed toolpath generation algorithm demonstrates scalable computational performance, further accelerated through CPU-based parallel

processing using the Intel MKL library [54]. Table 1 summarises the computational cost for all tested models, showing that computation times remain manageable even for final spatial toolpaths containing over 496.8 k waypoints, with an input tetrahedral mesh of 255.8 k elements. In our implementation, the mesh density is determined according to the model size and was set to make average edge length at 1.2 mm to balance between computational efficiency and toolpath accuracy.

5.2. Materials and robot-assisted ESP setup

The robot-assisted multi-axis embedded silicone printing platform used in this study is shown in Figure 10. The system integrates a six degrees-of-freedoms (DOFs) UR5e robotic arm, a mechanical screw-driven extrusion module, and a support bath to enable

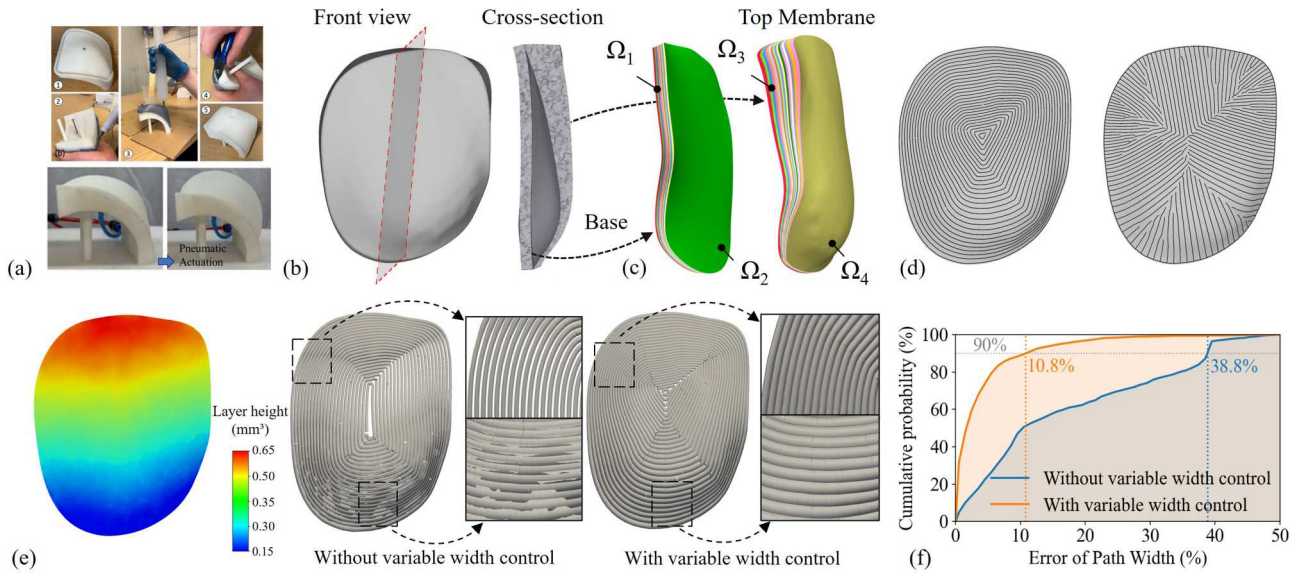


Figure 9. (a) The conventional molding process for fabricating deformable membranes requires substantial manual labour (figure reproduced from [48], ©IEEE). (b) The mannequin chest model with inner free-form cavity represented by a two-layer tetrahedral mesh. (c) Slicing result with preservation of critical surfaces Ω_1 – Ω_4 . (d) Staggered toolpath computed on odd and even layers. (e) Left: distribution of local layer heights within a single layer. Right: with deformation-based width control, issues of over- and under-extrusion are eliminated. For visualisation purposes, the toolpath cross-section is computed from the waypoint speed following Figure 2, where the cross-sectional height corresponds to the local layer height. (f) Cumulative distribution of path-width error with/without width-based deformation.

precise free-form fabrication. The support bath is prepared by dissolving 0.5wt% Carbomer ETD2020 in deionised water, followed by pH neutralisation with NaOH and vacuum degassing. The two-component silicone inks consists of: Part A mixed with 1.5wt% THIN-VEX (3wt% for Ecoflex-0030) as a thickening agent, and Part B mixed with 1wt% Slo-Jo as a retarder. All silicone components are provided by SmoothOn but with different mechanical characteristics. Specifically, Ecoflex 0030 exhibits a Shore 00 hardness of 30 and a tensile strength of 200 psi. In contrast, Dragon Skin 10 shows a Shore A hardness of 10 with a tensile strength of 471 psi, whereas Dragon Skin 30 exhibits a Shore A hardness of 30 and a tensile strength of 420 psi.

Prior to printing, both components are pre-loaded into individual syringes and driven by compressed air into a dual-liquid screw extruder (Model 600, Company Xinhui Automation Technology Co., Ltd.), which ensures continuous and precisely metered

mixing. The extrusion rate is regulated by a dedicated extruder controller interfaced with the host computer via an Ethernet connection. As discussed in Section 3.2, the extrusion rate is kept constant along the printing at $6.57 \text{ mm}^3/\text{s}$.

To achieve coordinated robot-extruder motion, we provide a motion-planning method that synchronises material extrusion with nozzle kinematics. The robot's trajectory is generated from a series of waypoints (as defined in Equation (16)), where the desired end-effector velocity is computed and mapped into joint space by solving the differential kinematics using the manipulator Jacobian [55]. The solution is executed in real time through RoboDK [56] software (as shown on the PC monitor in Figure 10), which communicates velocity and position commands to the UR5e controller. This closed control loop ensures smooth multi-axis movement and stable material flow, allowing accurate spatial deposition and reliable control of the local material distribution.

Table 1. Statistics of tested models and computing time.

Models	Figure	Model size (mm)	Tet #	Computing time of (Sec.)		Layer #	Total time (Sec.)
				Curved slicing	Spatial toolpath Comp.		
Prosthetic socket	Figure 1	$137 \times 125 \times 212$	255.8 k	57.2	198.5	340	255.7
Soft robot	Figure 7	$40 \times 40 \times 200$	207.3 k	37.2	29.6	400	66.8
Aorta phantom	Figure 8	$90 \times 24 \times 200$	115.5 k	15.1	20.8	300	35.9
Mannequin chest	Figure 9	$82 \times 100 \times 28$	197.5 k	11.9	64.2	24	76.1

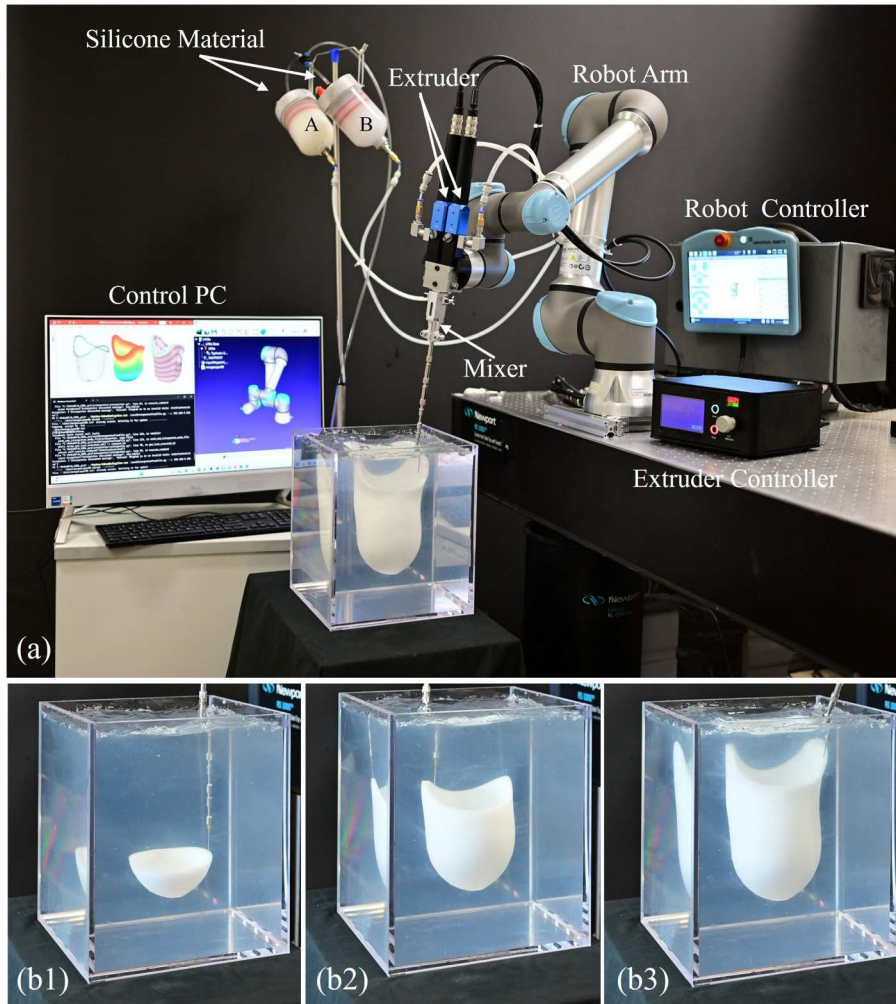


Figure 10. (a) Physical experiment setup of multi-axis ESP, where a 6-DOF robot arm is used to provide spatial material extrusion with synchronised motion along the extruder. (b) Fabrication process of the prosthetic socket model.

5.3. Fabrication result and characterisation

With the assistance of multi-axis motion from the robotic arm and precise synchronisation of micro-motor-driven extrusion, the computed spatial toolpaths for the models are fabricated, achieving accurate geometry and fulfilling their intended functions as free-from solid structures. All details of the physical printing process and physical validation can be found in the supplemental video. Notably, the spatial toolpaths with staggered patterns exceptionally ensure air-tightness for models designed for pneumatic actuation. The results for the soft robots are shown in Figure 11, where the cross-section demonstrates that our method prevents local accumulation of excessive ink in solid areas. The thin-wall sections exhibit relatively uniform wall thickness, while the solid sections are fully dense and void-free, indicating that the staggered toolpath effectively provides infill. As shown in Figure 11(b-d), these soft robots were fabricated with Ecoflex 0030 exhibit distinct deformation

behaviours under low pressure, where the thin-wall regions expand under inflation, enabling the robots to exhibit different deformation patterns, such as bending and twisting under pressures of 6.5 kPa, 5 kPa, and 7 kPa, respectively. Importantly, the proposed method is compatible with multiple silicone materials possessing different rheological and mechanical properties (as discussed in Section 3.1). Shown in Figure 11(e,f), S-shaped robots printed using Mold Star 30 and Dragon Skin 10 also maintained stable morphology and air-tightness. Under the same pressure of 18 kPa, the softer one displays a larger bending curvature. These observations demonstrate that the proposed method enables reliable fabrication of complex soft devices from a wide range of materials, thereby offering strong versatility and scalability for different functional and mechanical design requirements.

The successful fabrication of free-form soft membranes is demonstrated in Figure 12, where the

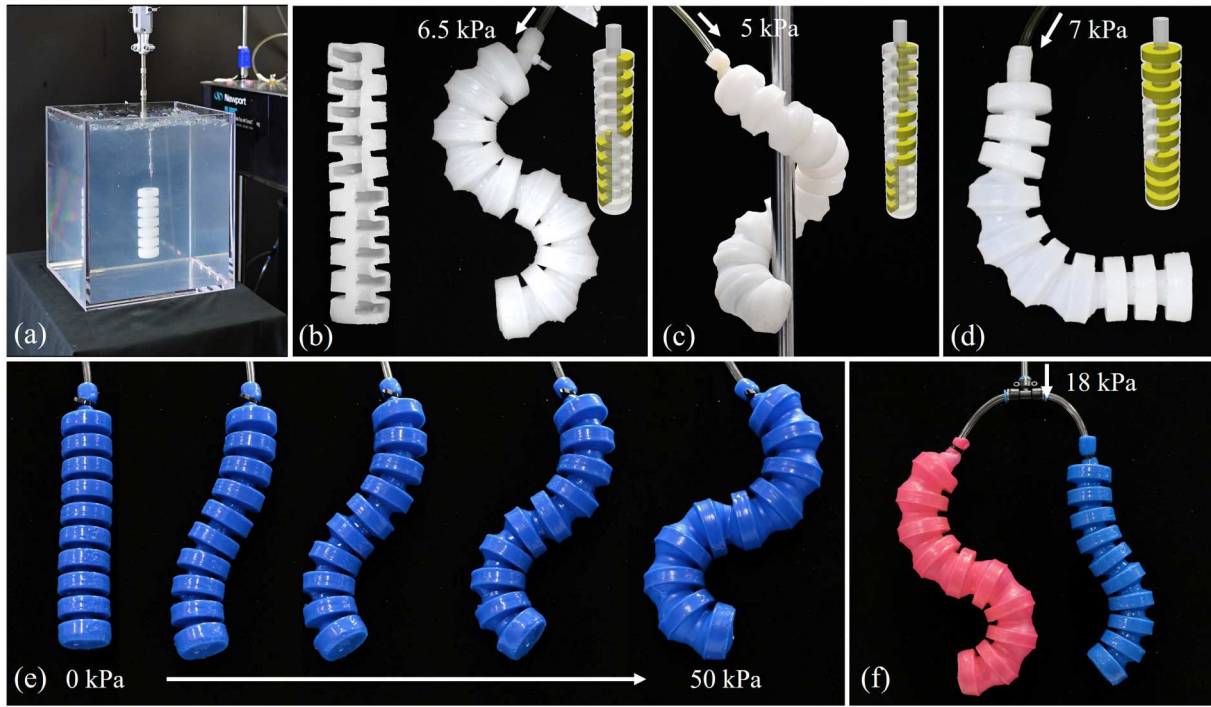


Figure 11. Printing results of soft robot models with various silicone materials. (a) printing process with robot-assisted ESP; (b) Longitudinal cross-section of S-shaped soft robot and its inflated shape; (c) inflated twisting-type and (d) L-shaped soft robots; all three robots were fabricated from Ecoflex 0030 but with different internal designs. (e) Deformation of the S-shaped soft robot made from Mold Star 30 under different pressures; and (f) Deformation of S-shaped soft robots made from Dragon Skin 10 (left) and Mold Star 30 (right) under the same pressure.

multi-axis printing process is showcased. As shown in Figure 12(a2) and (a3), the top layer of the base and the bottom layer of the top membrane successfully form a free-form chamber. The caved support gel is removed after printing when the air supply tube is extracted. The printed model is then placed on a solid PLA base, and when inflated with 10 kPa pressure, the

constant-thickness model expand into an approximately spherical shape (Figure 12(b1)). In contrast, the variable-thickness model inflates into a morphology more closely resembling the human chest (Figure 12(b2)). Before and after inflation, the model can replicate chest morphologies corresponding to different body types, as shown in Figure 12(c), and the surface shapes before

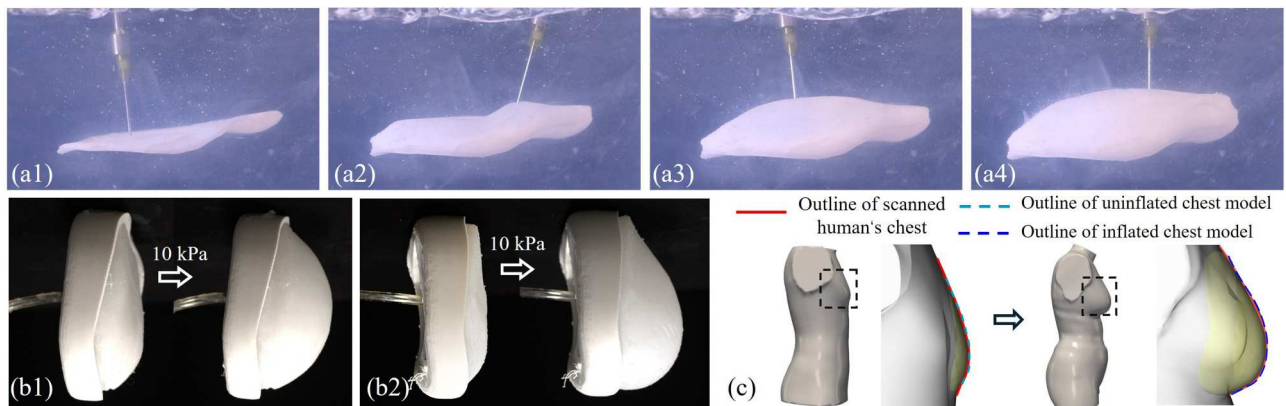


Figure 12. (a) Multi-axis ESP process of a two-layer chest model with variable thickness where (a2) highlights the process formulation enclosed pneumatic chamber (detail can also be found in supplemental video). (b) The chest models present different shapes after inflation. Left: chest model with constant thickness; Right: chest model with variable thickness design (i.e. computational result shown in Figure 9) can better mimic the human chest shape and it allows the shape change from (c) human chest shape 1 (left) to human chest shape 2 (right).

and after deformation were validated using a 3D scanner. This confirms that our proposed multi-axis ESP method significantly enhances design freedom for free-form surfaces.

The physical fabrication of the aorta model is demonstrated in Figure 13. It can be seen that critical regions with large printing angles are protected with high surface finishing with the help of multi-axis motion, which ensures good material fusion and proper silicone extrusion using the computed spatial toolpath. We validated the fabricated models using both 3D scanner (for outer surface) and CT imaging (for internal porosity analyses). As shown in Figure 13(c2), the 3D scanner results reveal a high degree of geometric conformity between the printed model and the original design, with the surface error less than 1.5 mm (1 % of the model size). Additionally, the CT scans provide detailed cross-sectional imaging and porosity analyses (Figure 13(c3)), demonstrating the ability of the designed toolpath to achieve excellent infill performance with minimal voids (pore ratio: 0.25%). These results confirm that the proposed multi-axis motion and toolpath planning method can successfully produce complex geometries with high precision and structural integrity.

We also demonstrate the effectiveness of the proposed method compared with the planar-based solution, where the toolpath is generated by commercial software (e.g. Cura [57]). As shown in Figure 13(b), the conventional ESP toolpath resulted in inferior printing quality. As can be seen in the zoom-in region, for the top part, distinct over- and under-deposition defects are observed due to the absence of a volume-preservation strategy. In addition, noticeable staircase effect and stringing defects appear on the printed surface due to the discontinuity of the toolpath. By comparing the dimensional error maps shown in Figure 13(b2) and (c2), it can be observed that the proposed multi-axis ESP method achieves markedly higher printing accuracy than conventional ESP, with the average error reduced from 0.49 mm to 0.2 mm, corresponding to a 59 % improvement in dimensional accuracy.

The stability and reproducibility of the proposed printing process were evaluated by repeatedly fabricating the aorta model over multiple cycles. As shown in Figure 13(d), the error distributions from multiple print cycles are highly consistent, confirming the stable performance of our method for complex silicone structures. These results demonstrate that the proposed multi-axis motion and toolpath-planning strategy can reliably

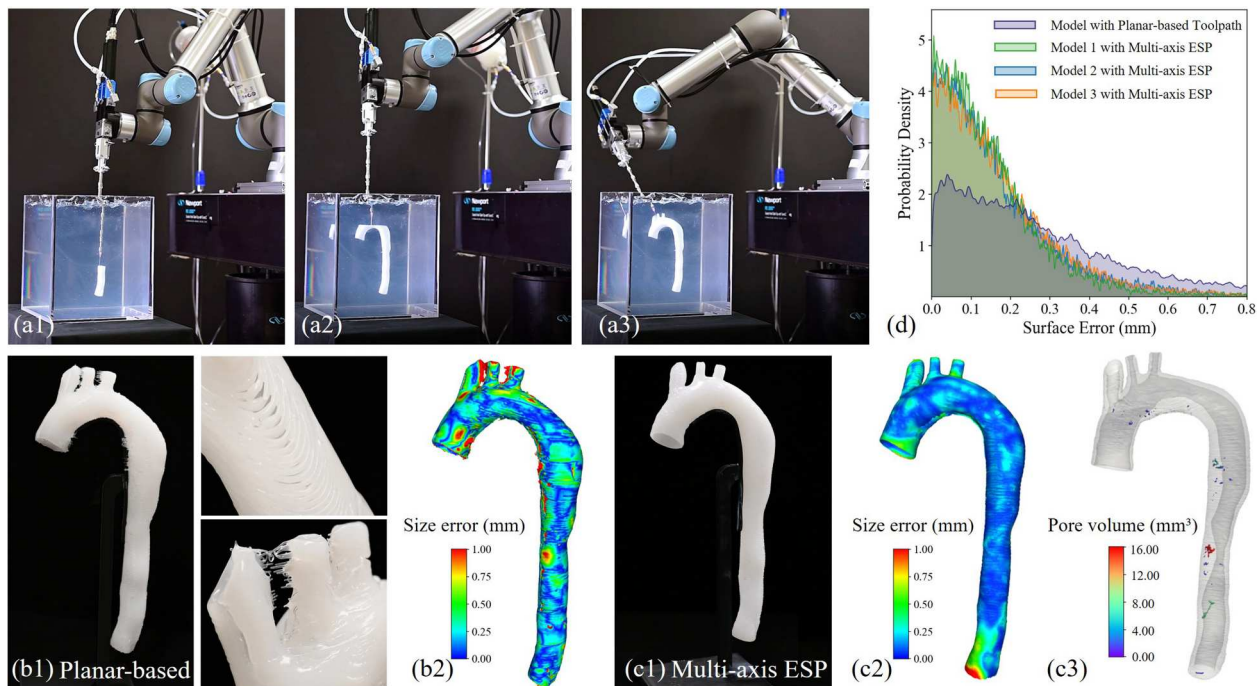


Figure 13. (a) Multi-axis ESP process of the aorta model, where the spatial motion of the robot enables conformal printing to protect critical regions. (b) Printed result of conventional planar-based ESP shows improper ink deposition and obvious stringing defects in the critical region, which results in a larger dimensional error. (c) Printed result of our method showing good surface finishing, high geometry accuracy, and good infill performance – as evidenced by the CT scanning result in (c3). (d) Error distributions from multiple printing cycles. The three multi-axis printing cycles demonstrate excellent consistency and repeatability. Compared with conventional planar ESP, the multi-axis printing achieves higher dimensional accuracy, reducing the average error from 0.49 mm to 0.20 mm.

achieve high precision and structural integrity in complex geometries. This stability highlights the potential of our approach to support mass production of silicone phantoms for biomedical applications. Furthermore, the MRI signal characteristics of different tissues can be replicated by tuning the infill density during printing [58]. Although ESP may introduce more infill defects than conventional DIW when fabricating solid volumetric parts, it offers a distinct advantage: the ability to print tall, free-form, and anatomically accurate structures without distortion or collapse, making it particularly suitable for advanced MRI phantom fabrication.

5.4. Discussion

With the support of experiment result, we have demonstrated that the width-constrained staggered toolpath can effectively promote more uniform ink distribution on curved layers with variable layer heights. However, due to the inherent characteristics of ESP, local ink over-deposition and pores caused by residual matrix material cannot be completely avoided, particularly in regions with complex geometry with sharp changes in local volume. Moreover, compared with thin-wall structure printing, volumetric printing using ESP requires more extensive nozzle movements, and the frequent motion of the nozzle may pull or disturb the surrounding matrix in three-dimensional space, potentially affecting the printed features and leading to manufacturing defects. A potential solution is the introduction of an in-situ monitoring system (e.g. the one reported for DIW [59]) to evaluate the printing process in real time and dynamically adjust printing parameters to compensate for these inconsistencies, which represents an important direction for future exploration.

Another challenge arises from potential collisions between the printing nozzle and the material tank, especially when fabricating surfaces with large slopes or steep curvature. In this work, we employed a 6-DOF robotic arm to maintain a constant printing angle and ensure uniform filament morphology. However, when printing large-scale objects, collision avoidance and nozzle-orientation constraints together restrict the achievable printing size. A straightforward approach is to adjust the nozzle geometry based on the local surface orientation. For example, switching between different nozzle configurations, such as the 45° or 90° nozzle designs introduced in [12], can help prevent interference by maintaining an optimal approach angle relative to the surface. On the other hand, advanced computational tool need to be developed to better place the model accordingly to the robotic position, reduce the potential of collision for this case.

Future work will extend the proposed framework to more diverse support matrix material and structures with greater geometric complexity [60, 61]. By integrating enhanced material compatibility with advanced spatial toolpath planning, the framework can broaden its range of applications. These capabilities will further enable the fabrication of complex functional soft devices, such as perceptive robots and biological tissues, thereby advancing the design freedom and overall performance of soft robotic and biomedical systems. Additionally, incorporating multi-material ESP [10, 41] together with the spatial printing proposed in this work would further enhance printing flexibility and reliability, particularly for fabricating functional and geometrically complex soft devices.

6. Conclusion

In this work, we presented a robot-assisted multi-axis embedded silicone printing platform capable of fabricating high-fidelity volumetric models with minimised geometric distortion and eliminating staircase artifacts on curved surfaces. The proposed computational framework couples curved-layer slicing, printing-direction planning, and width-constrained toolpath generation to ensure uniform material distribution and continuous filament deposition across complex geometries. Through the integration of high-DOF robotic motion and an ink-volume control mechanism, stable extrusion and accurate layer formation were achieved within a gel-based support medium. Experimental validation demonstrated that the printed structures closely matched their target designs, confirming the system's ability to achieve solid infill, smooth surfaces, and consistent material fusion. This work greatly broadens the applicability of ESP toward fully volumetric free-form manufacturing and demonstrates its effectiveness in producing customised functional soft systems.

Notes

1. Their material properties are shown in Figure 2.
2. Available at <https://doi.org/10.5281/zenodo.17596817>.

Acknowledgments

The authors would like to thank the technical team at Rapid Liquid Printing (RLP) for insightful discussions during the initial stage of this project, and the anonymous reviewers for their valuable comments. The authors acknowledge the support of the Chinese University of Hong Kong, the Hong Kong SAR Research Grants Council Early Career Scheme, and the Shenzhen basic research key project.Hailin Sun:

Writing – original draft, Visualization, Validation, Software, Methodology, Investigation, Formal,analysis, Data curation, Conceptualization. Yingjun,Tian: Visualization, Resources, Software, Methodology, Data curation, Conceptualization, Writing – review and,editing. Chenyu Xu: Visualization, Resources, Software, Writing – review and editing. Mahdi Bodaghi: Investigation, Methodology, Writing – review and editing. Fei,Gao: Data curation, Conceptualization, Funding acquisition, Writing – review and editing. Guoxin Fang: Writing – review and editing, Writing – original draft, Supervision, Methodology, Investigation, Funding acquisition, Formal analysis, Conceptualization.

Disclosure statement

No potential conflict of interest was reported by the author(s).

Funding

This research was supported by the Shun Hing Institute of Advanced Engineering at the Chinese University of Hong Kong (MMTp12-25), the Hong Kong SAR Research Grants Council Early Career Scheme (RGC-ECS) (CUHK/24204924), and Shenzhen basic research key project (Project No. JCYJ20220818101407016).

Author contributions

CRediT: **Hailin Sun:** Conceptualization, Data curation, Formal analysis, Investigation, Methodology, Software, Validation, Visualization, Writing – original draft; **Yingjun Tian:** Data curation, Methodology, Resources, Software, Visualization, Writing – review & editing; **Chenyu Xu:** Resources, Software, Visualization, Writing – review & editing; **Mahdi Bodaghi:** Investigation, Methodology, Writing – review & editing; **Fei Gao:** Conceptualization, Data curation, Funding acquisition, Writing – review & editing; **Guoxin Fang:** Conceptualization, Funding acquisition, Methodology, Project administration, Resources, Supervision, Visualization, Writing – original draft, Writing – review & editing.

Data availability statement

The raw test data (generated sliced layer and toolpath) supporting the findings of this study are openly available in Zenodo at: <https://doi.org/10.5281/zenodo.17596694>.

The supplemental video of this work can be found at: <https://doi.org/10.5281/zenodo.17596817>.

ORCID

Hailin Sun  <http://orcid.org/0000-0002-7251-2860>
Yingjun Tian  <http://orcid.org/0000-0002-9213-2179>
Chenyu Xu  <http://orcid.org/0009-0001-2808-2664>
Mahdi Bodaghi  <http://orcid.org/0000-0002-0707-944X>
Fei Gao  <http://orcid.org/0000-0001-9637-6114>
Guoxin Fang  <http://orcid.org/0000-0001-8741-3227>

References

- [1] Shit SC, Shah P. A review on silicone rubber. National Acad Sci Lett. 2013;36(4):355–365. doi: [10.1007/s40009-013-0150-2](https://doi.org/10.1007/s40009-013-0150-2)
- [2] Khas KS, Pandey PM, Ray AR. Rapid manufacturing of a clubfoot model imitating soft tissue and bones. Virtual Phys Prototyp. 2013;8(3):187–192. doi: [10.1080/17452759.2013.836455](https://doi.org/10.1080/17452759.2013.836455)
- [3] Mohammed MI, Cadd B, Peart G, et al. Augmented patient-specific facial prosthesis production using medical imaging modelling and 3d printing technologies for improved patient outcomes. Virtual Phys Prototyp. 2018;13(3):164–176. doi: [10.1080/17452759.2018.1446122](https://doi.org/10.1080/17452759.2018.1446122)
- [4] Pfeil S, Katzer K, Kanan A, et al. A biomimetic fish fin-like robot based on textile reinforced silicone. Micromachines. 2020;11(3):298. doi: [10.3390/mi11030298](https://doi.org/10.3390/mi11030298)
- [5] Bell MA, Becker KP, Wood RJ. Injection molding of soft robots. Adv Mater Technol. 2022;7(1):2100605. doi: [10.1002/admt.v7.1](https://doi.org/10.1002/admt.v7.1)
- [6] Liravi F, Toyserkani E. Additive manufacturing of silicone structures: A review and prospective. Addit Manuf. 2018;24:232–242.
- [7] Yang Z, Zhu W, Shi J, et al. Rapid in-situ thermal curing 3d printing of engineering thermosetting resins. Virtual Phys Prototyp. 2025;20(1):e2553180. doi: [10.1080/17452759.2025.2553180](https://doi.org/10.1080/17452759.2025.2553180)
- [8] Zhao J, He N. A mini-review of embedded 3d printing: supporting media and strategies. J Mater Chem B. 2020;8(46):10474–10486. doi: [10.1039/DOTB01819H](https://doi.org/10.1039/DOTB01819H)
- [9] Zeng X, Meng Z, Qiu Z, et al. Melt-based embedded printing for freeform fabrication of overhanging and flexible polycaprolactone scaffolds. Virtual Phys Prototyp. 2023;18(1):e2209778. doi: [10.1080/17452759.2023.2209778](https://doi.org/10.1080/17452759.2023.2209778)
- [10] Li Y, Wu Z, Chen Y, et al. Multi-material embedded 3d printing for one-step manufacturing of multifunctional components in soft robotics. Addit Manuf. 2024;85:104178.
- [11] Calais T, Sanandiya ND, Jain S, et al. Freeform liquid 3d printing of soft functional components for soft robotics. ACS Appl Mater Interfaces. 2021;14(1):2301–2315. doi: [10.1021/acsmami.1c20209](https://doi.org/10.1021/acsmami.1c20209)
- [12] Wang Z, Zhang B, He Q, et al. Multimaterial embedded 3d printing of composite reinforced soft actuators. Research. 2023;6:0122. doi: [10.34133/research.0122](https://doi.org/10.34133/research.0122)
- [13] Sparrman B, Du Pasquier C, Thomsen C, et al. Printed silicone pneumatic actuators for soft robotics. Addit Manuf. 2021;40:101860.
- [14] Albert BJ, Wang C, Williams C, et al. Non-planar embedded 3d printing for complex hydrogel manufacturing. Bioprinting. 2022;28:e00242. doi: [10.1016/j.bprint.2022.e00242](https://doi.org/10.1016/j.bprint.2022.e00242)
- [15] Arun ND, Yang H, Yao L, et al. Nonplanar 3d printing of epoxy using freeform reversible embedding. Adv Mater Technol. 2023;8(7):2201542. doi: [10.1002/admt.v8.7](https://doi.org/10.1002/admt.v8.7)
- [16] Shojaei Barjuei E, Shin J, Kim K, et al. High-precision multi-axis robotic printing: optimized workflow for complex tissue creation. Bioengineering. 2025;12(9):949. doi: [10.3390/bioengineering12090949](https://doi.org/10.3390/bioengineering12090949)
- [17] Grosskopf AK, Truby RL, Kim H, et al. Viscoplastic matrix materials for embedded 3d printing. ACS Appl Mater

- Interfaces. 2018;10(27):23353–23361. doi: 10.1021/acsami.7b19818
- [18] Hua W, Zhang C, Mitchell K, et al. Filament formation mechanisms in yield-stress fluid-enabled embedded ink writing. *Addit Manuf.* 2024;91:104353.
- [19] Bhattacharjee T, Zehnder SM, Rowe KG, et al. Writing in the granular gel medium. *Sci Adv.* 2015;1(8):e1500655. doi: 10.1126/sciadv.1500655
- [20] Song K, Compaan AM, Chai W, et al. Injectable gelatin microgel-based composite ink for 3d bioprinting in air. *ACS Appl Mater Interfaces.* 2020;12(20):22453–22466. doi: 10.1021/acsami.0c01497
- [21] Jin Y, Song K, Gellermann N, et al. Printing of hydrophobic materials in fumed silica nanoparticle suspension. *ACS Appl Mater Interfaces.* 2019;11(32):29207–29217. doi: 10.1021/acsami.9b07433
- [22] Rapid Liquid Print. Rapid liquid print; 2024 [accessed 2024 Jul 12]. Available from: <https://www.rapidliquidprint.com/>
- [23] Menon A, Póczos B, Feinberg AW, et al. Optimization of silicone 3d printing with hierarchical machine learning. *3D Printing Addit Manuf.* 2019;6(4):181–189. doi: 10.1089/3dp.2018.0088
- [24] Greenwood TE, Hatch SE, Colton MB, et al. 3d printing low-stiffness silicone within a curable support matrix. *Addit Manuf.* 2021;37:101681.
- [25] Zhao J, Hussain M, Wang M, et al. Embedded 3d printing of multi-internal surfaces of hydrogels. *Addit Manuf.* 2020;32:101097.
- [26] Young CA, O'Bannon M, Thomson SL. Three-dimensional printing of ultrasoft silicone with a functional stiffness gradient. *3D Printing Addit Manuf.* 2024;11(2):435–445. doi: 10.1089/3dp.2022.0218
- [27] Kubalak JR, Wicks AL, Williams CB. Using multi-axis material extrusion to improve mechanical properties through surface reinforcement. *Virtual Phys Prototyp.* 2018;13(1):32–38. doi: 10.1080/17452759.2017.1392686
- [28] Ye J, Guo Q, Lu H, et al. Topology optimisation of self-supporting structures based on the multi-directional additive manufacturing technique. *Virtual Phys Prototyp.* 2023;18(1):e2271458. doi: 10.1080/17452759.2023.2271458
- [29] Huang J, Ware HOT, Hai R, et al. Conformal geometry and multimaterial additive manufacturing through freeform transformation of building layers. *Adv Mater.* 2021;33(11):2005672. doi: 10.1002/adma.v33.11
- [30] Dai C, Liu T, Guo D, et al. Curve-based slicer for multi-axis dlp 3d printing. *ACM Trans Graphics (TOG).* 2025;44(6):194–14doi: 10.1145/3763352
- [31] Fang G, Zhang T, Huang Y, et al. Exceptional mechanical performance by spatial printing with continuous fiber: curved slicing, toolpath generation and physical verification. *Addit Manuf.* 2024;82:104048.
- [32] Gao S, Liao W-H, Guo P. Development of a multi-directional metal 3d printing system based on direct metal deposition. In: International Manufacturing Science and Engineering Conference, Vol. 58745. Erie (PA): American Society of Mechanical Engineers; 2019. p. V001T01A014.
- [33] Goh GL, Dikshit V, Koneru R, et al. Fabrication of design-optimized multifunctional safety cage with conformal circuits for drone using hybrid 3d printing technology. *Int J Advanced Manuf Technol.* 2022;120(3):2573–2586. doi: 10.1007/s00170-022-08831-y
- [34] Mendoza-Bautista KJ, Flores-Jimenez MS, Vázquez Tejeda Serrano LD, et al. Collaborative heterogeneous mini-robotic 3d printer for manufacturing complex food structures with multiple inks and curved deposition surfaces. *Micromachines.* 2025;16(3):264. doi: 10.3390/mi16030264
- [35] Zhang Z, Wu C, Dai C, et al. A multi-axis robot-based bio-printing system supporting natural cell function preservation and cardiac tissue fabrication. *Bioactive Mater.* 2022;18:138–150. doi: 10.1016/j.bioactmat.2022.02.009
- [36] Hajash K, Sparrman B, Guberan C, et al. Large-scale rapid liquid printing. *3D Printing Addit Manuf.* 2017;4(3):123–132. doi: 10.1089/3dp.2017.0037
- [37] Duraivel S, Laurent D, Rajon DA, et al. A silicone-based support material eliminates interfacial instabilities in 3d silicone printing. *Science.* 2023;379(6638):1248–1252. doi: 10.1126/science.adc4441
- [38] Etienne J, Ray N, Panozzo D, et al. Curvislicer: slightly curved slicing for 3-axis printers. *ACM Trans Graphics (TOG).* 2019;38(4):1–11. doi: 10.1145/3306346.3323022
- [39] Guerra A, Fortunato GM, Bonatti AF, et al. A cylindrical slicing algorithm for four-axis non-planar bioprinting of complex geometries. *Int J Bioprinting.* 2025;11(2):494–509. doi: 10.36922/IJB025070053
- [40] Qu J, Huang Z, Guo D, et al. Inf-3dp: implicit neural fields for collision-free multi-axis 3d printing. *ACM Trans Graphics (TOG).* 2025;44(6):1–18. doi: 10.1145/3763354
- [41] Wang Z, Zhang B, Cui W, et al. Freeform fabrication of pneumatic soft robots via multi-material jointed direct ink writing. *Macromol Mater Eng.* 2022;307(4):2100813. doi: 10.1002/mame.v307.4
- [42] Fang G, Zhang T, Zhong S, et al. Reinforced fdm: multi-axis filament alignment with controlled anisotropic strength. *ACM Trans Graphics (TOG).* 2020;39(6):1–15. doi: 10.1145/3414685.3417834
- [43] Dutta N, Zhang T, Fang G, et al. Vector field-based volume peeling for multi-axis machining. *J Comput Inf Sci Eng.* 2024;24(5):051001. doi: 10.1115/1.4063861
- [44] Crane K, Weischedel C, Wardetzky M. The heat method for distance computation. *Commun ACM.* 2017;60(11):90–99. doi: 10.1145/3131280
- [45] Knöppel F, Crane K, Pinkall U, et al. Stripe patterns on surfaces. *ACM Trans Graphics (TOG).* 2015;34(4):1–11. doi: 10.1145/2767000
- [46] Zhang T, Liu T, Dutta N, et al. Toolpath generation for high density spatial fiber printing guided by principal stresses. *Composites Part B: Engineering.* 2025;295:112154. doi: 10.1016/j.compositesb.2025.112154
- [47] Liu L, Zhang L, Xu Y, et al. A local/global approach to mesh parameterization. In: Computer graphics forum, Vol. 27. Copenhagen: Wiley Online Library; 2008. p. 1495–1504.
- [48] Tian Y, Fang G, Petrus JS, et al. Soft robotic mannequin: design and algorithm for deformation control. *IEEE ASME Trans Mechatron.* 2022;27(4):1820–1828. doi: 10.1109/TMECH.2022.3175759
- [49] Zhong Z, Wang W, Lévy B, et al. Computing a high-dimensional euclidean embedding from an arbitrary smooth riemannian metric. *ACM Trans Graphics (TOG).* 2018;37(4):1–16. doi: 10.1145/3197517.3201369

- [50] Guennebaud G, Jacob B. Eigen v3.3; 2019 [accessed 2024 Aug 6]. Available from: <http://eigen.tuxfamily.org>
- [51] Fang Y, Guo Y, Wu B, et al. Expanding embedded 3d bio-printing capability for engineering complex organs with freeform vascular networks. *Adv Mater.* **2023**;35(22):2205082. doi: [10.1002/adma.v35.22](https://doi.org/10.1002/adma.v35.22)
- [52] Scharff RB, Fang G, Tian Y, et al. Sensing and reconstruction of 3-d deformation on pneumatic soft robots. *IEEE ASME Trans Mechatron.* **2021**;26(4):1877–1885. doi: [10.1109/TMECH.2021.3078263](https://doi.org/10.1109/TMECH.2021.3078263)
- [53] Li S, Xie B, Chen Y, et al. Design and 3d printing of lower limb prosthetic socket. In: 2024 IEEE International Conference on Cyborg and Bionic Systems (CBS). Nagoya: IEEE; 2024. p. 27–32.
- [54] Wang E, Zhang Q, Shen B, et al. Intel math kernel library. In: High-Performance Computing on the Intel® Xeon Phi™: How to Fully Exploit MIC Architectures. Cham: Springer; 2014. p. 167–188.
- [55] Chen Y, Zhang T, Huang Y, et al. Co-optimization of tool orientations, kinematic redundancy, and waypoint timing for robot-assisted manufacturing. *IEEE Trans Autom Sci Eng.* **2025**;22:12102–12117. doi: [10.1109/TASE.2025.3542218](https://doi.org/10.1109/TASE.2025.3542218)
- [56] Robodk. Robodk: simulator for robot arms and offline programming. Available from: <https://robodk.com/>
- [57] Ultimaker cura. Available from: <https://ultimaker.com/software/ultimaker-cura/>
- [58] Hatamikia S, Zaric O, Jaksa L, et al. Evaluation of 3d-printed silicone phantoms with controllable mri signal properties. *Int J Bioprinting.* **2025**;11(3):381–396.
- [59] Mejia EB, McDougall L, Gonsalves N, et al. Real-time process monitoring and automated control for direct ink write 3d printing of frontally polymerizing thermosets. *npj Adv Manuf.* **2025**;2(1):18. doi: [10.1038/s44334-025-00032-1](https://doi.org/10.1038/s44334-025-00032-1)
- [60] Wang X, Li Z, Deng J, et al. Unprecedented strength enhancement observed in interpenetrating phase composites of aperiodic lattice metamaterials. *Adv Funct Mater.* **2025**;35(1):2406890. doi: [10.1002/adfm.v35.1](https://doi.org/10.1002/adfm.v35.1)
- [61] Wang X, Li X, Li Z, et al. Superior strength, toughness, and damage-tolerance observed in microlattices of aperiodic unit cells. *Small.* **2024**;20(23):2307369. doi: [10.1002/smll.v20.23](https://doi.org/10.1002/smll.v20.23)